



**HAL**  
open science

# Nanocube epitaxy for the realisation of printable monocrystalline nanophotonic surfaces

Anna Capitaine, Beniamino Sciacca

► **To cite this version:**

Anna Capitaine, Beniamino Sciacca. Nanocube epitaxy for the realisation of printable monocrystalline nanophotonic surfaces. 2022. hal-03538271v1

**HAL Id: hal-03538271**

**<https://hal.science/hal-03538271v1>**

Preprint submitted on 26 Jan 2022 (v1), last revised 31 Mar 2022 (v2)

**HAL** is a multi-disciplinary open access archive for the deposit and dissemination of scientific research documents, whether they are published or not. The documents may come from teaching and research institutions in France or abroad, or from public or private research centers.

L'archive ouverte pluridisciplinaire **HAL**, est destinée au dépôt et à la diffusion de documents scientifiques de niveau recherche, publiés ou non, émanant des établissements d'enseignement et de recherche français ou étrangers, des laboratoires publics ou privés.

# Nanocube epitaxy for the realisation of printable monocrystalline nanophotonic surfaces

Anna Capitaine and Beniamino Sciacca\*

*Aix Marseille Univ, CNRS, CINaM, AMUtech, Marseille, France*

E-mail: beniamino.sciacca@cnrs.fr

## Abstract

Plasmonic nanoparticles of the highest quality can be obtained via colloidal synthesis at low-cost. Despite the strong potential for integration in nanophotonic devices, the geometry of colloidal plasmonic nanoparticles is mostly limited to that of Platonic solids. This is in stark contrast to nanostructures obtained by top-down methods, that offer unlimited capability for plasmon resonance engineering, but present poor material quality and have doubtful perspectives for scalability. Here, we introduce an approach that combines the best of the two worlds by transforming assemblies of single-crystal gold nanocube building blocks into continuous monocrystalline plasmonic nanostructures with an arbitrary shape, via epitaxy in solution at near ambient temperature. We used nanocube dimers as a nanoreactor model system to investigate the mechanism *in operando*. Measuring the collective optical response of  $\sim 40$  nanocube reactors revealed competitive redox processes of oxidative etching at the nanocube corners and simultaneous heterogeneous nucleation at their surface, that ensure the filling of the sub-nanometer gap in a self-limited manner. Tuning the experi-

mental parameters (temperature, pH, halide concentration) proved effective in controlling the morphology of the resulting monocrystalline nanostructures from (100) to (111) capping facets. Applying this procedure to nanocube arrays assembled in a patterned polydimethylsiloxane (PDMS) substrate, we are able to obtain printable monocrystalline nanoantenna arrays that can be swiftly integrated in devices. This could lead to the implementation of low cost nanophotonic surfaces of the highest quality in industrial products.

## Introduction

Controlling the geometry of individual nanostructures and their assembly into organized arrays, on a large area at low cost, is key to take nanophotonic and plasmonic devices from a laboratory scale to industrial products.<sup>1-3</sup> In particular, metal nanoparticles support surface plasmon resonances that are responsible for confining light to a dimension much smaller than the corresponding free-space wavelength and enable for large optical cross-sections.<sup>4-10</sup> As a result of this intense light confinement, the optical and electrical properties strongly depend on size, shape, material properties and dielectric environment. The unique features of plasmonic nanostructures has led to countless applications in various fields. As an example, supported on a substrate they have been proposed for surface-enhanced spectroscopy,<sup>11-14</sup> catalysis,<sup>15-17</sup> sensing<sup>14,18,19</sup> and diverse photonic applications<sup>20</sup> that take advantage of the properties of individual nanoparticles<sup>21</sup> or of the collective resonances of phased arrays<sup>6,8,22</sup> to name a few.

Control on the nanoscale geometry is commonly achieved by patterning thin films via lithography techniques followed by evaporation and lift-off processes or etching.<sup>23</sup> Such top-down nanofabrication steps not only are expensive, time consuming and hardly scalable, but produce materials that are polycrystalline, have substantial surface roughness or present damages as a result of etching. On the contrary, material quality is of paramount importance to building high efficiency optoelectronic and nanophotonic devices.<sup>6,24-26</sup> Therefore,

monocrystalline materials are ideal constituents to reach ultimate performance. However, this requirement adds further fabrication complexity owing to an epitaxial growth step to form a thin film prior to nanostructuring. This substantially restricts the integration to layers that are lattice-matched and that can withstand high temperature, vacuum<sup>24</sup> and possibly wet lift-off steps.<sup>27</sup>

Chemical syntheses on the other hand allow one to obtain high-quality colloidal nanoparticles, free of grain boundaries or stress that hamper electron conduction and weaken plasmon resonances.<sup>24,28</sup> A variety of shapes (nanowires, nanocubes, nanoplates, nanoflowers, nanoprisms, etc...) can be achieved by tuning the synthesis parameters or by particle attachment,<sup>29</sup> with extensive control of size and material composition. Nevertheless, gaining further control on the shape of nanocrystals beyond that of conventional Platonic solids, is crucial to introduce morphological anisotropy by design and tune the physicochemical properties to specific applications.<sup>30</sup> This hinders the realisation of nanophotonic surfaces having individual units with an arbitrarily complex geometry, that is often needed in plasmonics, and therefore limits substantially their potential.

Here we lift this barrier and take advantage of solution processed nanomaterials (nanocubes) to fabricate extended 1D and 2D monocrystalline nanostructure arrays of arbitrary shape (at near ambient temperature) and print them to any substrate. Single-crystal nanocubes are ideal building blocks because they have the highest intrinsic material quality and they have a 4-fold rotational invariance. This ensures identical crystallographic orientation of adjacent units, that is crucial to transform a discontinuous assembly into a continuous monocrystalline nanostructure via nanocube epitaxy.<sup>31</sup> This makes solution synthesis a promising route towards the fabrication of low cost nanophotonic surfaces of highest quality.

A variety of materials used for optoelectronic applications can be synthesized as single-crystal nanocubes in solution, as for example Ag, Au, Cu, Al<sup>32-34</sup> (metals) Cu<sub>2</sub>O, PbS, CsPbX<sub>3</sub><sup>35-37</sup> (semiconductors) and BiFeO<sub>3</sub>, SrTiO<sub>3</sub> and CeO<sub>2</sub><sup>38-40</sup> (dielectric), to name a few. Among them gold stands as an excellent candidate because it exhibits very good electrical and



optical properties, and it is a prime choice in many plasmonic and nanophotonic devices.<sup>6,41</sup> In addition, the excellent thermal and chemical stability enable to study nanocube epitaxy without interference from the environment, oxide layers or absorbed species.

First, we demonstrate that the strategy described above can be used as a general method to transform arbitrary assemblies of gold nanocubes (supported on a silicon substrate) into 1D and 2D monocrystalline nanostructures. This is enabled by the introduction of a novel approach of simultaneous oxidative dissolution and growth, that can also be used to control the faceting of the resulting continuous monocrystalline nanostructures by tuning few key parameters. Then, we show for the first time that by applying this procedure to nanocubes organized in polydimethylsiloxane (PDMS) via directed assembly, monocrystalline Au nanopatterns by design can then be transferred to virtually any kind of substrate. This paves the way for swift integration of nanophotonic surfaces of the highest quality in optical and optoelectronic devices and architectures that are incompatible with classic nanopatterning strategies such as perovskite layers. Finally, we extensively study the chemical framework for nanocube epitaxy with a set of controlled experiments *ex-situ* and *in operando* on a nanocube dimer model system. This provides with invaluable insights on the mechanism with atomic scale resolution.

## **Welding of adjacent nanocubes on silicon**

Gold nanocubes (30 to 40-nm) are synthesized following the procedure earlier reported by Park *et al.*<sup>28</sup> The solutions are highly monodisperse, and when dropcasted on a substrate nanocubes self-assemble face-to-face in a 2D closed-packed configuration, separated by a gap smaller than 1 nanometer (Figure S1, Figure S14). This constitutes an ideal platform to study nanocube epitaxy, as the product can swiftly be characterized with scanning electron microscopy (SEM).

After deposition, nanocubes are extensively washed to remove adsorbed molecules resid-

ual from the synthesis and obtain a pristine surface.<sup>31,42</sup> If exposed to a solution containing a gold precursor ( $\text{HAuCl}_4$ ) and a weak reductant (ascorbic acid), adjacent nanocubes grow and merge producing continuous gold nanostructures (Figure S2). Unfortunately, reduction of  $\text{AuCl}_4^-$  in the bulk of the solution leads to homogeneous nucleation, causing contamination of the sample with small nanocrystals and inefficient use of reactants. We therefore explored the opportunity to achieve nanocube epitaxy in the absence of a reducing agent, so that  $\text{AuCl}_4^-$  ions can reach the nanocubes surface without being consumed in the bulk of the solution.

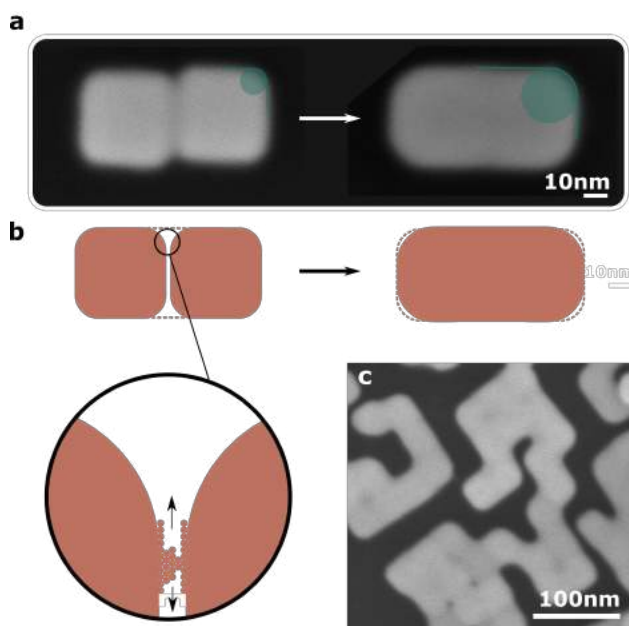


Figure 1: Epitaxial welding of gold nanocubes on silicon using a solution of  $\text{HAuCl}_4$  only. a) SEM image of two 40-nm ligand-free nanocubes on silicon before (left) and after exposure to a  $80\mu\text{M}$   $\text{HAuCl}_4$  solution at  $40^\circ\text{C}$  for 5 minutes (right); the green circles represent the radius of curvature. b) Schematic representation of the welding. c) SEM image of self-assembled 32-nm nanocubes after ligand removal and welding with a  $80\mu\text{M}$   $\text{HAuCl}_4$  solution at  $40^\circ\text{C}$  for one second.

Figure 1 presents evidence of nanocube epitaxy at near ambient temperature, for 32 nm and 40 nm nanocubes (panel c and a, respectively) achieved using a solution of  $\text{HAuCl}_4$   $80\mu\text{M}$  only. This concentration was found to give optimal results at a temperature of  $40^\circ\text{C}$  and these conditions will be used as reference in this article. The sub-nanometer gaps are successfully filled, yielding to continuous 1D and 2D nanostructures whose geometry

is directed by the position of the nanocubes prior to welding, with good shape and angle retention. The resulting 1D nanostructures (Figure 1a) are on average  $\sim 10\%$  wider compared to the nanocubes before welding, whereas the length is unchanged (Figure S14). This is key to the realization of nanostructures that have an arbitrary geometry with control down to the nanometer scale. The radius of curvature increases after welding (see statistics in Figure S14), which is attributed to oxidative etching of the nanocube corners, and it is amplified as the  $\text{HAuCl}_4$  concentration increases or when  $\text{Cl}^-$  ions are added to the solution (see next). Besides preventing homogeneous nucleation and avoiding sample contamination with small nanocrystals, we found that this strategy is robust, as it leads to successful welding over a wide range of  $\text{HAuCl}_4$  concentration ( $1 \mu\text{M}$  -  $10 \text{ mM}$ ), reaction temperature (room temperature (RT) -  $80^\circ\text{C}$ ) and pH, with a time scale from less than a second (Figure 1c) to a few minutes, despite the fact that no reductant is introduced in the solution.

## Printable monocrystalline nanoantenna arrays

Applying the welding procedure on gold nanocubes organized in arrays and tuning the welding parameters (temperature, pH, introduction of halide ions) enable us to realize monocrystalline nanopatterned surfaces with extensive morphology control, that is especially important for plasmonics and nanophotonics. The low surface energy of PDMS makes it a convenient support for nanostructures self-assembly and growth, and ensures that those can be later released to virtually any substrate by contact printing (Figure 2a). Micro and nanoparticles can be assembled in nanostructured PDMS using capillary assembly.<sup>43-47</sup> Silicon masters were patterned using e-beam lithography and used to fabricate PDMS moulds with traps designed to accommodate a certain number of nanocubes in a given geometry. Using this technique we realized periodic arrays of 2, 3, 4, 5 and 8 nanocubes as a proof of concept (Figure 2b and S12), but there is no limit to the geometry that can be obtained.

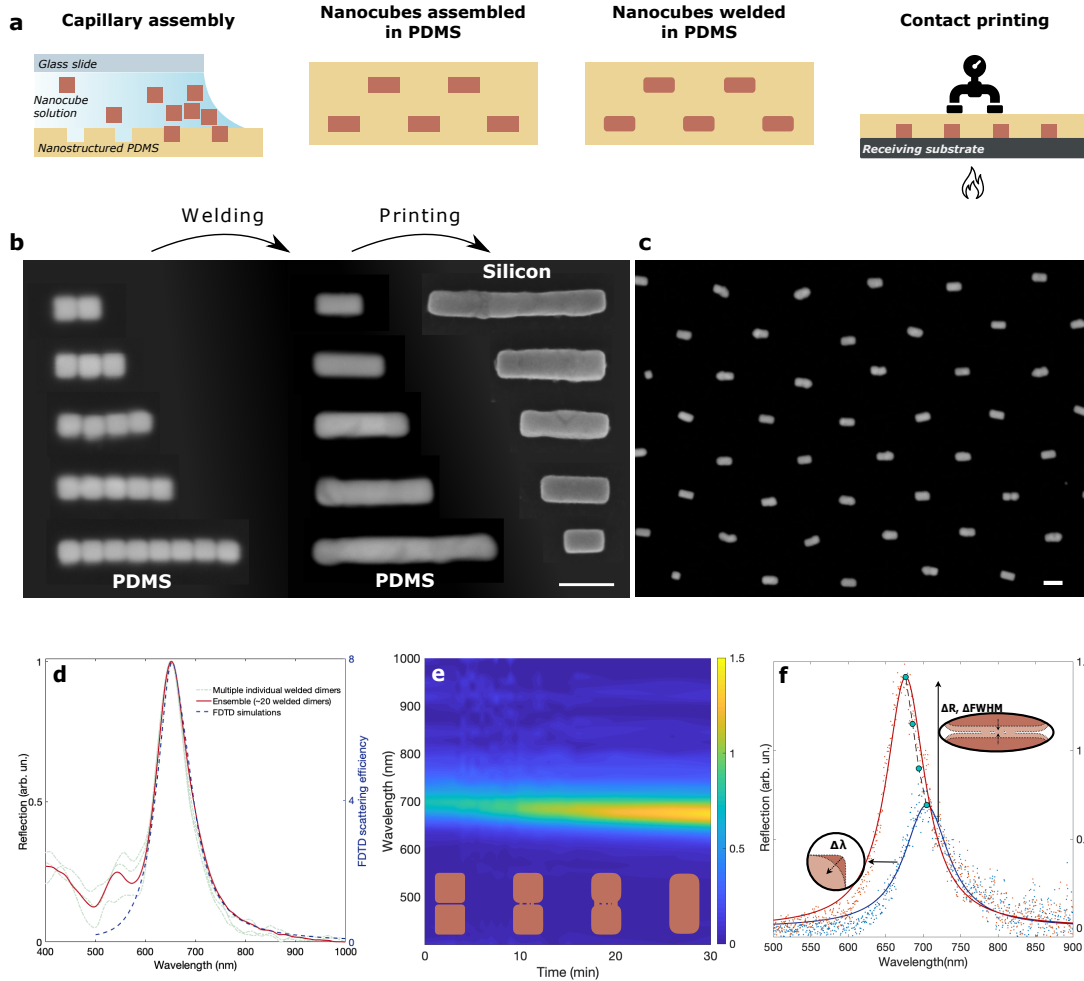


Figure 2: Realization of monocrystalline nanostructures by design on PDMS. a) Illustration of the process: capillary assembly in nanopatterned PDMS, nanocube epitaxy in solution and printing of monocrystalline nanostructures to any substrate. b) Collage of SEM images taken from large arrays made of 2, 3, 4, 5 and 8 nanocubes, showing 40 nm gold nanocubes assembled into 1D nanostructures of arbitrary length in PDMS before nanocube epitaxy (left image), after nanocube epitaxy in PDMS (middle image) and after printing to a silicon substrates (right image). c) SEM image of nanoantenna arrays on PDMS after nanocube epitaxy. d) Optical response (unpolarized light) of multiple individual nanoantennas (dotted line) and nanoantenna array (solid line) supported on PDMS, showing the intense dipolar longitudinal mode at 680 nm and the transverse mode at 550 nm. Realistic FDTD simulations of the nanoantenna array in PDMS (blue dashed line, polarisation parallel to the dimer long axis); the agreement with experimental data in terms of resonance position and full-width-half-max (FWHM) confirms the realisation of a material of the highest quality. e) Nanocube epitaxy on a model system *in operando*. An ensemble of  $\sim 40$  dimers in an array configuration on PDMS (panel c) is probed during epitaxy performed at RT; inset: diagram illustrating the evolution of nanocube dimers into a continuous welded bar. f) Data in panel d at the beginning ( $t = 0$  s) and at the end ( $t = 30$  min) of nanocube epitaxy, and the corresponding Lorentzian fits (solid lines). The green dots represent the resonance position at intermediate times. The blue-shift, the increase in intensity of the dipolar mode and the narrowing of the linewidth testify changes of the system morphology at the atomic scale. The scale bar in SEM images is 100 nm.

The welding procedure using  $\text{HAuCl}_4$  only optimized for nanocubes supported on a silicon substrate did not yield consistent results on different substrates, such as glass,  $\text{Si}_3\text{N}_4$  or PDMS, most likely due to differences in surface chemistry and surface energy that impact the local reaction environment (more detail in SI). Results on silicon revealed that two mechanisms were at play: oxidation of the nanocube corners and gold reduction at the surface. Slight modification of the welding procedure, by performing the reaction at pH 1 (to promote oxidation) and introducing micromolar concentrations of NaBr (to enhance (100) facets reactivity<sup>48</sup>) enabled gold nanocube epitaxy on all substrates, including PDMS, transforming the welding procedure developed on silicon into a general solution route towards continuous monocrystalline nanostructures of arbitrary shape (Figure 2b). Figure 2c illustrates a periodic array of gold nanoantennas (with an aspect ratio of 2) obtained via nanocube epitaxy on a PDMS substrate. The sample exhibits homogeneous welding and very good shape retention throughout the entire substrate ( $200\ \mu\text{m} \times 200\ \mu\text{m}$ ). The optical response of individual nanoantennas and of an ensemble are compared in Figure 2d. The reflection peak at 680 nm corresponds to the longitudinal dipolar mode. It is worth to note that (i) different individual dimers show approximately the same behaviour, (ii) the collective response of an ensemble of  $\sim 20$  dimers is almost identical to that of individual dimers, (iii) the resonance linewidth and position are in extraordinary agreement with Finite Difference Time Domain (FDTD) simulations, indicating a material of the highest quality. This provides evidence that nanocube epitaxy enables the realisation of bottom-up nanophotonic surfaces, with an exquisite control of position and geometry of individual resonators (comparable to e-beam lithography), and a material quality superior to what can be achieved with metal evaporation, that is the standard approach in nanofabrication.

The regular geometry of the nanoantenna array constitutes an ideal platform to examine nanocube epitaxy *in operando*, permitting to probe simultaneously the optical response of a number of nanoreactors. The strong light confinement in plasmonic nanoparticle systems allows extraordinary sensitivity to their geometry and their environment.<sup>21</sup> Compared to

other *in operando* techniques, such as liquid-phase TEM, optical approaches ensures minimal perturbation, that is especially important to study redox chemical reactions. We will show that this can be used to access information on nanocube epitaxy, with atomic resolution.

Figure 2e presents the kinetics of nanocube epitaxy, corresponding to the collective reflection of  $\sim 40$  dimers nanoreactors supported on PDMS, starting from the exposure to the welding solution to complete epitaxy. The main features that can be evidenced in the kinetics response are illustrated in Figure 2f: i) the blue-shift of the dipolar mode is associated with the rounding of the nanocube corners, ii) the increase of the mode intensity and its linewidth narrowing correspond to an increase of conductivity between the isolated nanocubes as welding takes place. The nanogap is slowly filled with new adatoms that eventually provide an increasing number of electrical connections (bridges) between the two nanocubes. The multiplication of conduction pathways effectively reduces the resistance encountered by plasmons travelling in the dimer. The gradual disappearance of this (ohmic) loss channel boosts the dipolar mode intensity and narrows its linewidth. This is consistent with theoretical predictions on the spectral response of silver nanocube dimers as a function of the gap conductivity and radius of curvature of the corners.<sup>49</sup> These findings suggest that the two processes take place simultaneously (more details below), and contain the signature of changes of the atomic arrangement inside a sub-nanometer gap with unprecedented resolution.

Finally, such monocrystalline nanophotonic surface can be transferred from PDMS to other substrates for integration in optoelectronic devices, or for further characterisation. Figure 2b, shows nanoantennas of different lengths deposited from PDMS to silicon. During this process, the PDMS stamp is pressed against a receiving substrate, and the nanostructures are released due to the larger adhesion forces. It is worth noticing that the bottom surface of the nanoantennas, initially in contact with PDMS, also exhibit a continuous, gap-free surface. The nanoantenna arrays were printed from PDMS to a  $\text{Si}_3\text{N}_4$  membrane for high-resolution TEM (HRTEM) characterization. HRTEM images on different locations

and electron diffraction on the whole nanostructure are presented in Figure 3. These provide evidence (i) for a perfect crystallographic alignment of the two nanocubes at the time of assembly, (ii) for epitaxy between individual building blocks, and (iii) that the junction is filled in its entirety yielding gap-free monocrystalline nanostructures. In addition, we noticed that epitaxy can be achieved also in the presence of non-cubic nanoparticles (defects) with a different crystallographic orientation, and result in the formation of a grain boundary (Figure S13). This could promote grain boundaries engineering and trigger new material-by-design approaches.<sup>50,51</sup>

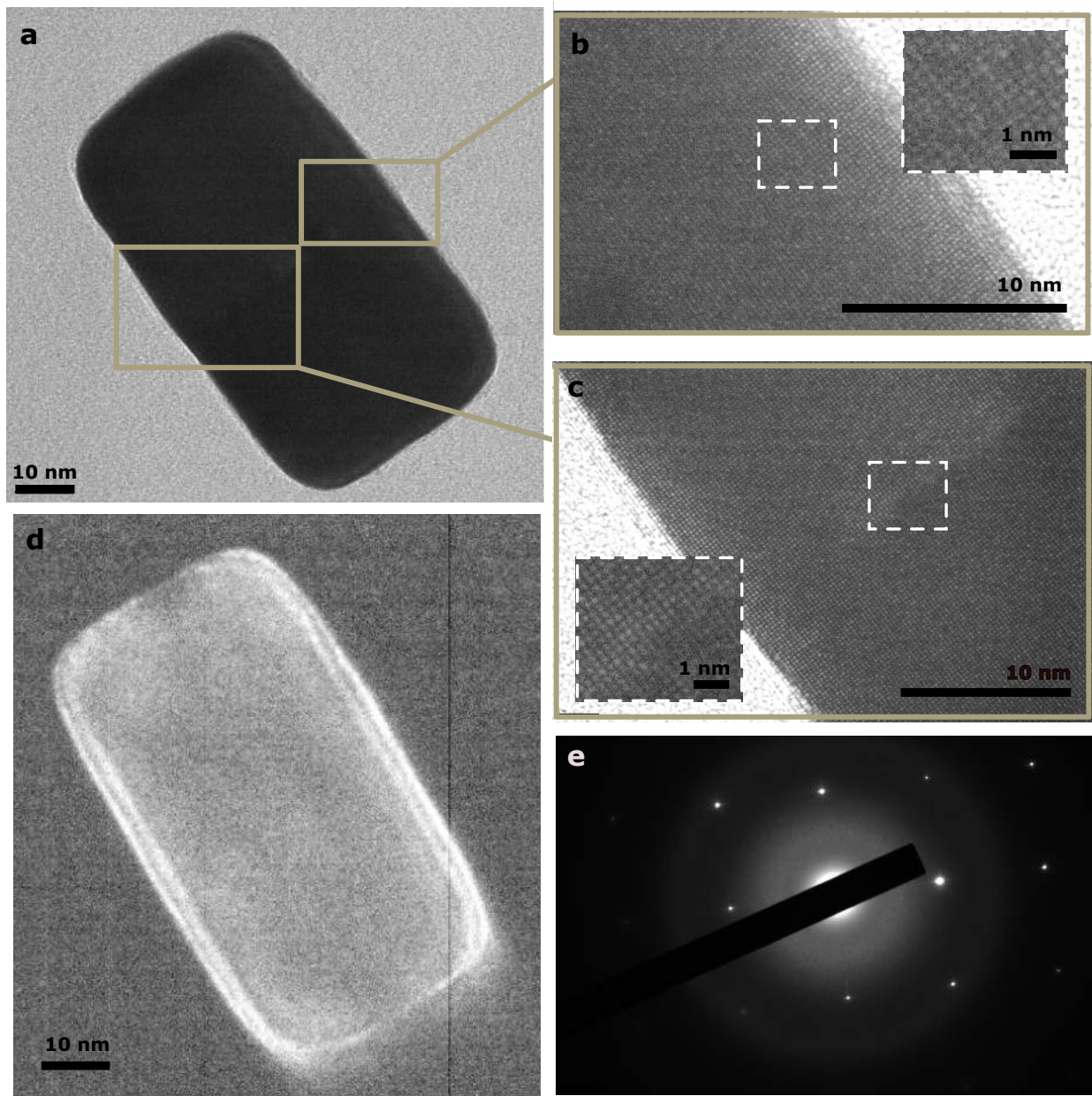


Figure 3: TEM characterization of the dimer arrays after epitaxy. a) Bright-field image. b), c) HRTEM showing a continuous gap-free material at the approximate location of where the junction between two nanocubes was before welding. d) Dark-field image showing no contrast at the junction. e) Electron Diffraction over the dimer showing the typical pattern of a single-crystal.



## Unveiling the mechanism of nanocube epitaxy

A number of control experiments were carried out to establish the framework of nanocube epitaxy and shine light on the mechanism. Thermodynamics drives a system to lower its total free energy, which ultimately controls the equilibrium shape of nanostructures, although kinetic barriers have to be overcome in most circumstances. In the case of two touching, ligand-free nanocubes, the total free energy is reduced if the dimer welds in a continuous bar, as a result of the disappearance of two surfaces. However, from TEM analysis we observed that, on average, adjacent nanocubes were separated by a gap corresponding to  $\sim 2x$  the lattice constant, that is sufficient to prevent spontaneous welding at RT (Figures S7, S8).

In the previous section we hypothesized that two mechanisms were at play: heterogeneous nucleation on the nanocubes (growth) and oxidative etching.

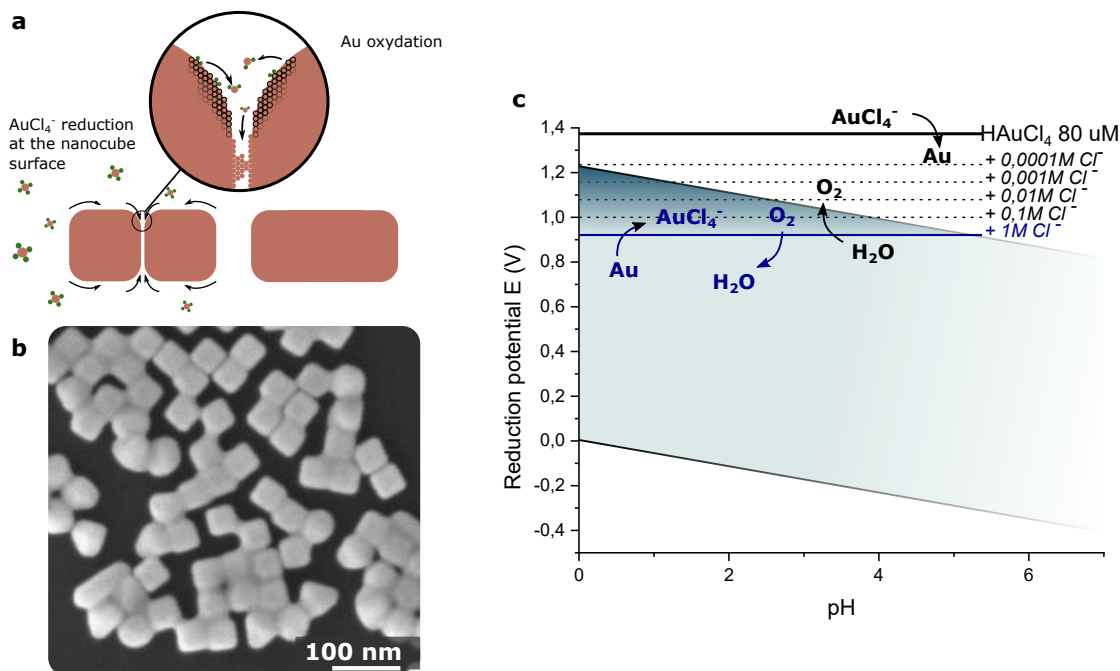
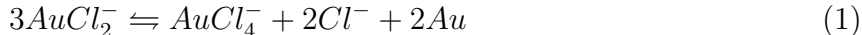


Figure 4: Insight into the welding mechanism. a) Illustration of the welding mechanism exhibiting simultaneous oxidation and growth. b) 40 nm gold nanocubes on silicon, partially welded using micromolar NaCl concentration only at 40°C. c) Pourbaix diagram of  $\text{AuCl}_4^-/\text{Au}(0)$  redox couple for  $\text{AuCl}_4^-$  concentration of 80  $\mu\text{M}$  at RT (black line). The green area shows the stability domain of water, while the dashed and blue line correspond to  $\text{AuCl}_4^-/\text{Au}(0)$  reduction potential in the presence of chloride.

In Figure 4c we present the Pourbaix diagram to illustrate the thermodynamic equilibrium of the the  $\text{AuCl}_4^-/\text{Au}(0)$  redox couple as a function of pH. While there should be no stability domain for Au(III) species ( $\text{AuCl}_4^-$ ) in our experimental conditions (black solid line), increasing  $\text{Cl}^-$  concentration and reducing pH can drive the system to a chemical equilibrium in which  $\text{AuCl}_4^-$  species are stable in solution, and therefore oxidative dissolution (corrosion) can take place. The strong binding affinity of chloride ions towards (111) and (110) facets<sup>30</sup> implies an enhanced reactivity of nanocube corners and edges towards oxidative dissolution. This is qualitatively validated with a set of experiments summarized in Figures S3, S4, S5, showing that rounding of nanocube corners is more pronounced at larger  $\text{Cl}^-$  concentration and lower pH. The apparent quantitative disagreement with the

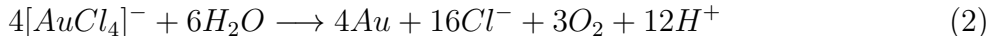
Pourbaix diagram can be explained by considering that as a result of adsorption, the  $\text{Cl}^-$  concentration on the nanocube surface is substantially larger than in the bulk.

Studies on oxidative etching of gold nanoparticles in chlorinated solutions revealed that  $\text{AuCl}_2^-$  (Au(I)) was the main dissolution product.<sup>52-54</sup> It is however unstable at low temperature<sup>55,56</sup> and can disproportionate to  $\text{AuCl}_4^-$  and Au(0) at the nanocube surface (Equation 1).



From the macroscopic point of view this would result in the displacement of Au atoms via chlorinated species intermediates. To test this hypothesis and identify the role of  $\text{Cl}^-$ , we replaced the 80  $\mu\text{M}$   $\text{HAuCl}_4$  solution with a NaCl solution containing an equivalent concentration of free chloride (2.5  $\mu\text{M}$  - calculations are detailed in the supporting material) and observed partial welding (Figure 4b). This suggests that gold atoms effectively migrate from (111) and (110) facets to (100) facets (including the gap) via dissolution in the presence of  $\text{Cl}^-$  ions and redeposition, as illustrated in Figure 4a. It is worth noticing that this mechanism is in agreement with the interpretation of the optical characterization results presented in Figure 2f. Nevertheless, we were not able to achieve complete welding while securing the shape of the nanocubes using NaCl only. Therefore, when performing nanocube epitaxy in the  $\text{HAuCl}_4$  solution, part of the welding material is coming from the nanocubes but a fraction must come from the gold precursor. UV-Visible spectra performed on the welding solution after 1h at 40°C revealed a  $\sim 2\text{x}$  larger Au(III) consumption in the presence of the nanocube substrate, corroborating our hypothesis (Figure S10).

According to the Pourbaix diagram, in our experimental conditions it is thermodynamically possible for water to reduce Au (III) directly to Au (0) (Equation 2), or to Au (I), that can be further reduced to Au (0) or can disproportionate following Equation 1 (Figure S16).



Although this seems in stark contrast with the fact that gold chloride aqueous solutions are typically stable in ambient conditions, the Pourbaix diagram does not take into account the kinetics of the system. Previous research has shown that in certain experimental conditions (aerosol microdroplets or microwave reactors), water oxidation could even lead to the formation of gold nanoparticles from  $\text{HAuCl}_4$  solutions without reducing agents.<sup>4,57</sup>

In addition, we observed that in most experimental conditions the morphology of the nanostructures does not evolve after welding is complete, even if the substrate is left to react for longer time (Figure S11). This is the trademark of a self-limited reaction, and indicates that the equilibrium between oxidative etching and growth is reached once the gap has been filled.

## Controlling the morphology

The accurate choice of experimental parameters allows to shift this equilibrium and favor dissolution or growth, providing a useful knob to finely control the morphology of the nanostructures resulting from nanocube epitaxy. Figure 5e summarizes some key parameters that can be tuned to design a specific surface. For example, in addition to increasing chloride concentration or lowering the pH, higher  $\text{HAuCl}_4$  concentrations or smaller nanocubes have shown to favor oxidative etching over growth at longer reaction time, leading to smooth nanostructures (Figure S11, S3 and S4).

It was found that increasing the temperature gives rise to rough morphologies, due to stronger heterogeneous nucleation. As the reaction temperature increases from RT to 40°C, nanostructures with irregular surfaces and egg-box shape start to appear after welding, exhibiting the more stable (111) facets, as evidenced in Figure 5b. This effect is strengthened if the temperature is further increased to 60°C and 80°C (Figure S6). In the absence of surfactants or additives, the surface free energy of (111) facets is lower than that of (100) facets. This drives the reorganization of (100) capped nanostructures into (111) and their

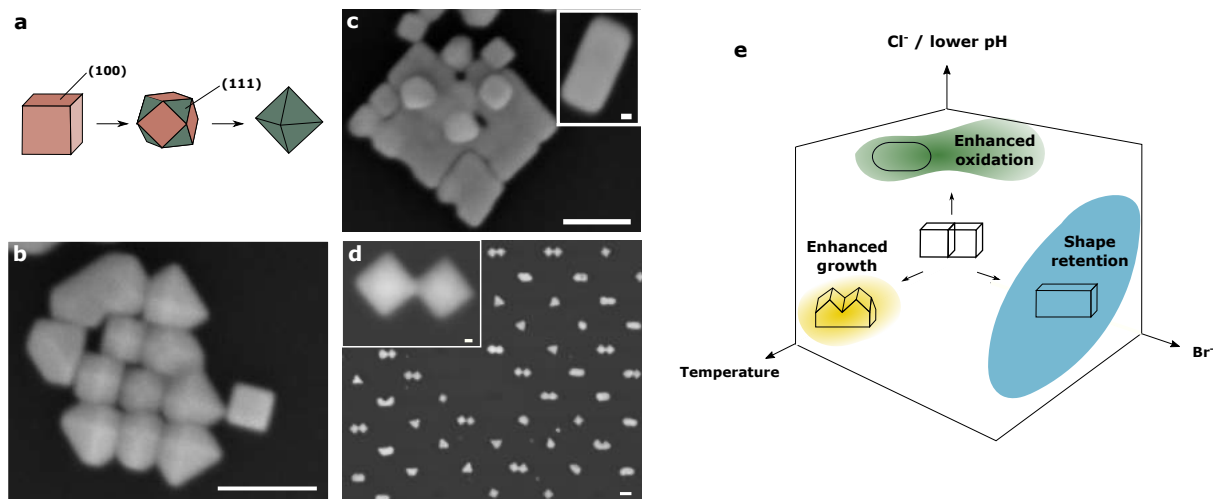


Figure 5: Control over the morphology. a) Schematic representation of (100) capped nanocube reshaping into (111) capped octahedron. b) SEM image of overgrown gold nanocubes on silicon after a one minute reaction with a  $80\mu\text{M}$   $\text{HAuCl}_4$  solution at  $40^\circ\text{C}$ . The (100) facets growth results in egg-boxes structures made of (111) facets. c) SEM image of a gold nanocubes welded by adding small quantities of NaBr to the welding solution. d) SEM image of overgrown gold nanocubes after assembly on PDMS at  $80^\circ\text{C}$ . e) Schematic summary of the effect of experimental conditions on the nanostructure morphology. The scale bar is 100 nm in the main images and 10 nm in the insets.

intermediates, as illustrated in Figure 5a. Figure 5b shows that in our conditions, only the surfaces that are not blocked by the substrate or the surrounding nanocubes are able to evolve towards (111) facets. As a result, nanocubes standing on the side of the self-assembly are prone to more transformation. The larger volume after the reaction confirms that growth takes place on (100) facets exposed to the welding solution despite the absence of a reductant.

Nanocube epitaxy performed at higher temperature exhibited faster kinetics and better results compared to RT. This induced us to investigate the opportunity to control the evolution equilibrium between (100) and (111) facets and achieve smooth surfaces even at higher temperature. Figure 5c shows that the introduction of  $\text{Br}^-$  ions at micromolar concentration promotes nanocube epitaxy at higher temperature while stabilizing (100) facets. Bromine ions are commonly used in nanocube synthesis to direct crystal growth because they bind to (100) facets, reducing their surface energy and growth rate.<sup>28,48</sup> Finally, it is important to note that morphology engineering during nanocube epitaxy can be used to transform dimer

arrays assembled in PDMS into bowtie arrays made of two facing octahedras capped with (111) facets, as shown in Figure 5d. The low surface energy of PDMS presumably allowed reshaping of all nanocube facets including the one in contact with PDMS itself. This is a proof of concept that engineering of complex nanoantenna morphologies can be achieved via bottom-up methods.

## Outlook

We have shown for the first time that gold monocrystalline nanostructure arrays of arbitrary shape could be fabricated via a bottom-up approach, using nanocubes as building blocks. This report challenges conventional approaches in the fields of plasmonics and crystal growths. In the former, focus is either put on the fabrication of plasmonic structures of average material quality with accurate control of the nanoscale geometry via top-down techniques, or on colloidal nanoparticles of high material quality enabled by low cost bottom-up chemical synthesis. In the latter, single crystal ingots are obtained from the melt using one single-crystal seed, whereas monocrystalline thin films are obtained via epitaxy in vacuum on substrates with the same lattice parameter. The results presented in this article represent a considerable step forward compared to the state of the art of these fields, and they have the potential to foster different research avenues. They show that monocrystalline gold nanostructures can be simply obtained via nanocube epitaxy at near ambient temperature from many single-crystal seeds (nanocubes) that could be assembled deterministically. This is especially important because the organisation of nanocubes before epitaxy determines the final shape of the monocrystalline nanostructure, allowing spatial resolution comparable to e-beam lithography, but with a process that has a strong potential from the technological perspective. The absence of a reducing agent simplifies the process substantially and avoids homogeneous nucleation of nanoparticles that would otherwise deteriorate the optical properties of the plasmonic surface. Optical measurements confirmed the excellent mate-

rial quality and showed a strong reproducibility of process. In addition, unlike conventional nanofabrication techniques where the (polycrystalline) nanostructures are fabricated directly on the substrate, we have shown that nanocube epitaxy can be performed directly on PDMS and that (monocrystalline) plasmonic surfaces by-design can be printed to any substrate, unleashing from lattice matching requirements. This is highly promising for the integration of monocrystalline gold nanostructures, such as transparent electrodes or plasmonic scatterers, in devices that are sensitive to temperature, water or other nanofabrication processes, as for example perovskite solar cells. Detailed analysis of the chemical landscape and optical spectroscopy in operando shone light on the nanocube epitaxy mechanism, revealing that gold atoms are displaced from the nanocube corners to the sub-nanometer gap via a self-limited redox reaction mediated by Cl<sup>-</sup> ions. Tuning this redox equilibrium allows to change the morphology of the nanostructures after epitaxy, transforming a nanocube dimer either into a continuous rectangular bar or into a bowtie element. The opportunity to configure the crystal facets during epitaxy widens the toolbox of geometries that can be achieved.

## Methods

### Material

PDMS was purchased from Wacker (RT601), HAuCl<sub>4</sub>, HNO<sub>3</sub>, NaBr, NaCl, NaBH<sub>4</sub> were purchased from Merck at the highest purity available.

## Gold Nanocube synthesis

Nanocubes were synthesized following Park et al. procedure.<sup>58</sup> Briefly, 10 nm CTAC-capped seeds were overgrown in a 50 mL round bottom flask using 6 mL of 100 mM CTAC, 30  $\mu$ L of sodium bromide at 40 mM, 100  $\mu$ L of the 10 nm seed solution at 2 OD in 20 mM CTAC, 390  $\mu$ L 10 mM ascorbic acid and 6 mL of 0.5 mM HAuCl<sub>4</sub> solution. The solution was left to react for 25 minutes at RT with gentle stirring prior to centrifugation. The nanocube solution was washed twice and redispersed in 10 mL of ultrapure water.

## Ligands removal

Substrate-supported nanocubes were first successively dipped into water, acetone, IPA for one minute each and rinsed with ultrapure water. Ligands adsorbed on the nanocube surface (CTAC, SDS, Triton-X45 residual from the synthesis or the assembly solution) were removed by adapting a procedure reported in.<sup>42</sup> Briefly the samples were immersed into a 100 mM NaBH<sub>4</sub> solution for 30 minutes, rinsed thoroughly and stored in ultrapure water until welding.

## Nanocube epitaxy on silicon

Typically 2  $\mu$ L of the nanocube solution in water was dropcasted on a silicon substrate. Ligands were removed after complete evaporation of the solution with the procedure described above. Welding was performed by introducing the silicon substrate into an HAuCl<sub>4</sub> solution with concentrations ranging from 1  $\mu$ M to 10 mM, at a temperature between RT and 80°C between 1 second and one hour using a water bath, with no agitation. The standard welding reaction on silicon was performed at 40°C with 80  $\mu$ M HAuCl<sub>4</sub>. Upon welding substrates were rinsed with ultrapure water and N<sub>2</sub> dried.



# Nanocube epitaxy on PDMS after capillary assembly

## Master fabrication

The silicon master was fabricated with e-beam lithography using PMMA resist on silicon. Upon exposition and development, a thin layer of chrome was evaporated on the substrate to be used as a hardmask. PMMA was then lifted-off in acetone. Silicon was then etched by 40 nm using Reactive Ion Etching (RIE). Chrome was finally removed using a commercial chrome etchant.

After oxygen plasma, the silicon master was silanized with perfluorodecyltrichlorosilane at room temperature in a desiccator for 20 minutes to ease PDMS demolding.

PDMS moulds were fabricated on a glass slide by depositing liquid degassed PDMS (commercial monomer and polymerizing agent mixed to a 9:1 ratio) on the silicon master and covering it by a glass slide. Upon reticulation of PDMS at 100°C for 10 minutes on a hot plate, the PDMS template was demolded from the silicon master. The PDMS moulds were then stored in ethanol for at least a few days prior to assembly to remove un-reacted species in PDMS.

## Capillary assembly

The nanocube solution was centrifuged at 9,000 RPM for 10 minutes and redispersed in 10 mL of 0.75 mM SDS and 0.0075 wt.% Triton X45. Assembly was performed by dragging the nanocube solution (50  $\mu\text{L}$ ) with a glass slide fixed 1 mm above the PDMS substrate, in a home-made system. The speed was set at 1  $\mu\text{m}\cdot\text{s}^{-1}$ , the temperature at 55°C and the humidity at 40%.<sup>45</sup>

## Nanocube epitaxy on PDMS

Assemblies were left to fully dry in air for at least an hour before removing the ligands with the strategy described above. When dipping the samples in  $\text{NaBH}_4$  right after assembly, part of the assembly would come off the substrate. Welding was performed by introducing the PDMS substrate into a solution containing  $80 \mu\text{M}$   $\text{HAuCl}_4$ ,  $50 \mu\text{M}$   $\text{NaBr}$  and  $100 \mu\text{L}$  of  $\text{HNO}_3$  to lower the pH to 1. Reaction was performed at  $40^\circ\text{C}$  for one hour, with no agitation. Upon welding substrates were rinsed with ultrapure water and dried with a stream of nitrogen.

## Printing

Printing was performed on silicon substrates and  $\text{Si}_3\text{N}_4$  TEM grids. The silicon substrate was treated with oxygen plasma for 10 minutes ( $200\text{W}$ ,  $150^\circ\text{C}$ ) before printing.  $5 \mu\text{L}$  of ethanol was deposited on silicon at  $20^\circ\text{C}$  and the PDMS sample was lowered manually and pressed onto the silicon substrate. The whole process was monitored using optical microscope by looking through the transparent PDMS, to ensure for good contact between the two substrates and to position assembled areas on silicon. When the two substrates were fully in contact, the temperature was then raised and maintained at  $50^\circ\text{C}$  for 10 minutes for the ethanol to dry. Upon releasing the pressure nanocubes remained in the silicon for which they have more affinity. The  $\text{Si}_3\text{N}_4$  TEM grids were used as purchased without plasma treatment. Because they cannot handle much pressure without breaking,  $1 \mu\text{L}$  of PMMA was deposited on the TEM grids to increase their adhesion, which allowed to print the nanocube assemblies with good resolution. Upon contact with PDMS, PMMA was pushed out of the sample which allowed imaging.

## Characterization and simulations

Assemblies of nanocubes on PDMS were imaged using a scanning electron microscope (JEOL 7900F) in low vacuum mode with a pressure of 60 Pa. TEM and electron diffraction was performed with a JEOL 2100F. Optical characterisation was performed with an inverted microscope (Zeiss Axiovert 200M) with an air objective (100X, NA = 0.9) in reflection. The PDMS without nanoantennas was used as the reference to take into account of the spectral response of the system. Light was coupled into a 25  $\mu\text{m}$  optical fiber, yielding a collection spot diameter of 1.3  $\mu\text{m}$ . The commercial software Lumerical was used to simulate the response of individual gold nanoantennas. A total field scattered field source was used with the electric field polarized along the nanoantenna long axis. The nanostructure was placed on PDMS to simulate the experimental environment as accurately as possible. The nanostructure dimensions were defined accordingly with SEM images (Width = 44 nm, length = 84 nm, radius of curvature = 8 nm). The dielectric constant from Johnson and Christy was used for gold.

## Acknowledgement

The authors thanks M. Abbarchi for fruitful discussions and for carefully reading the paper, D. Chaudanson and A. Altié for support with TEM characterisation and F. Bedu for support with e-beam lithography. B. Sciacca thanks AMUtech, MITI CNRS (project COMPACT) and ANR (project MeMeNtO) for funding.

## Supporting Information Available

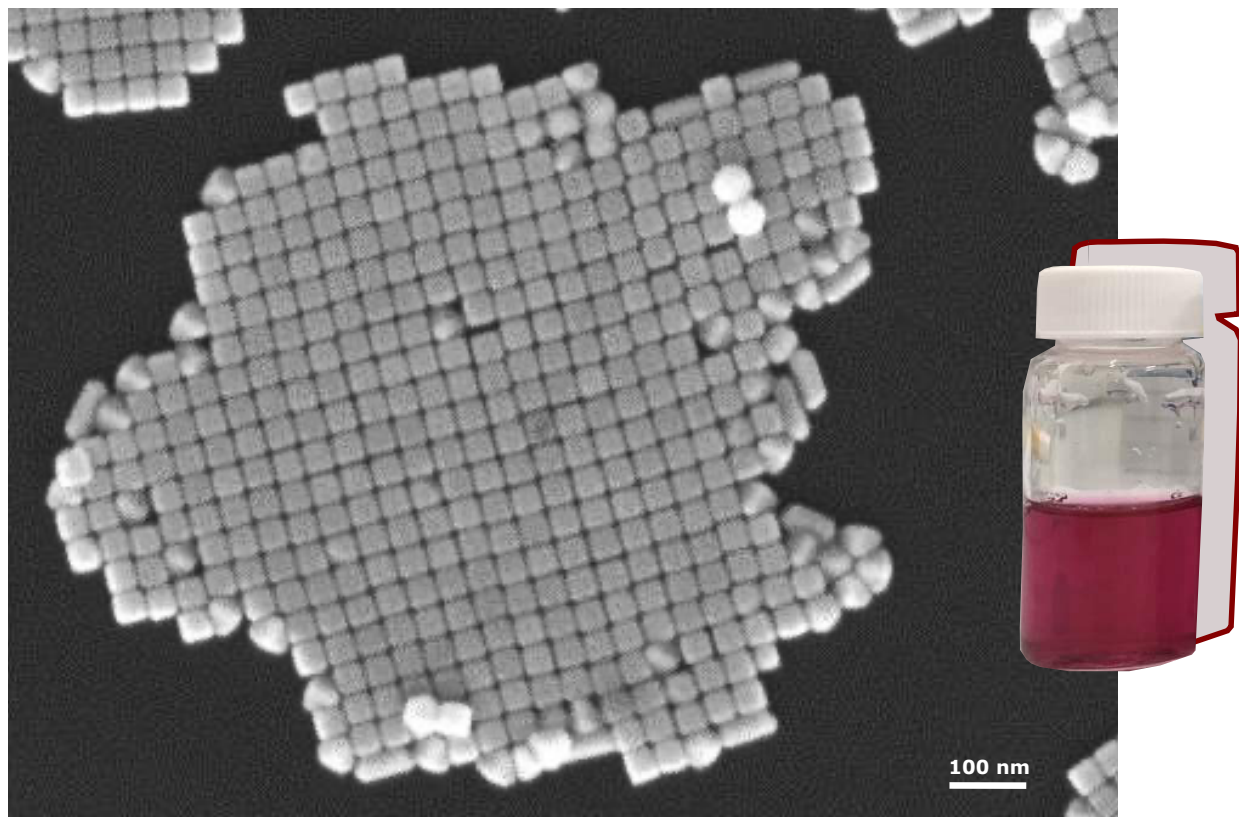


Figure S1: SEM image of self-assembled 40-nm gold nanocubes on silicon, synthesized by following Park et al. procedure.<sup>58</sup>

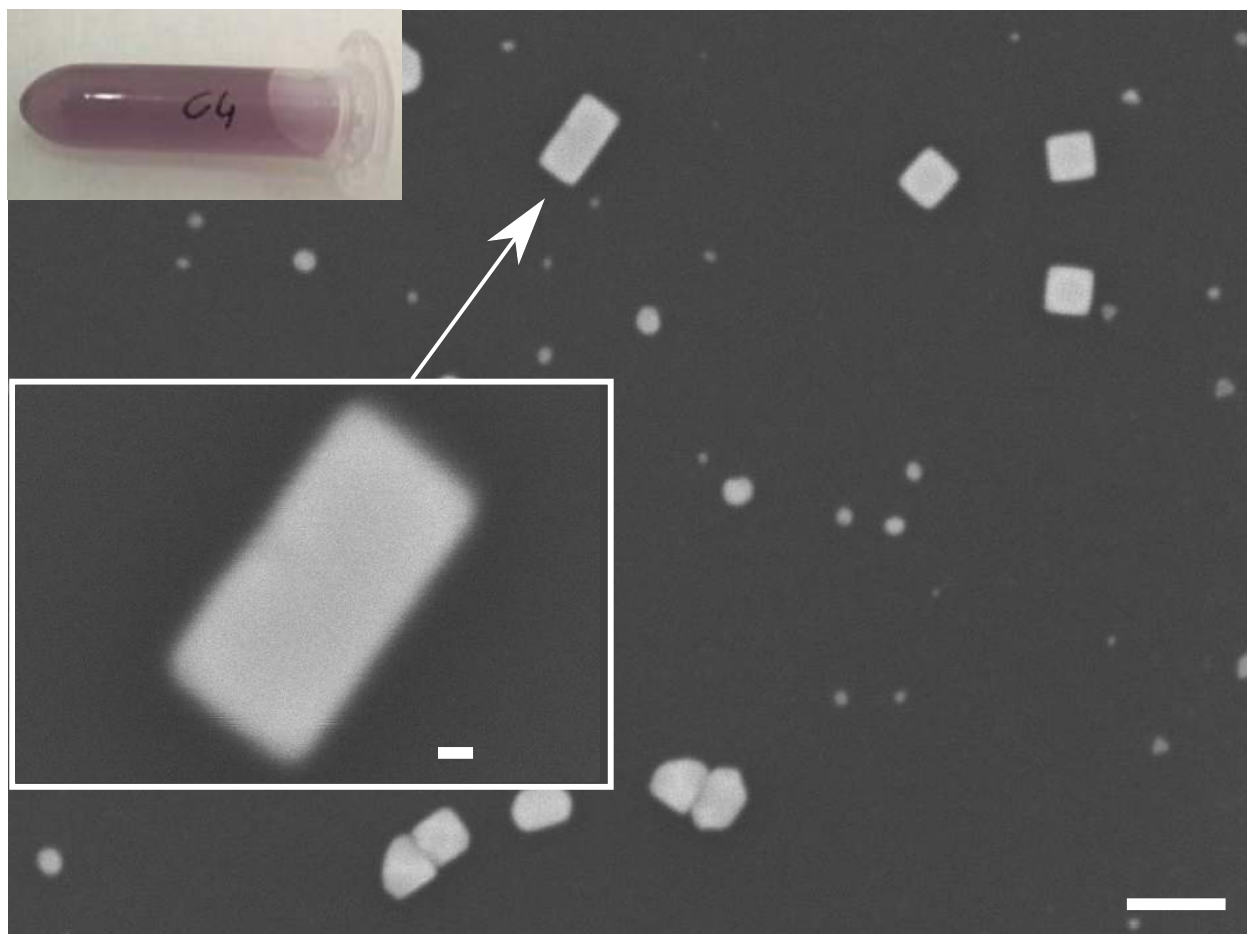


Figure S2: SEM image of 40 nm gold nanocubes on a silicon substrate after one minute reaction at room-temperature with a solution of  $\text{HAuCl}_4$  at  $300 \mu\text{M}$  and ascorbic acid at  $440 \mu\text{M}$ . Reduction of  $\text{HAuCl}_4$  by ascorbic acid allowed welding of two adjacent nanocubes as shown in the inset, however the silicon substrate was contaminated by nucleation from the solution. The photograph of the welding solution one minute after putting in contact, ascorbic acid,  $\text{HAuCl}_4$  and the nanocubes confirms the existence of homogeneous nucleation in solution. Scale bar is 100 nm.

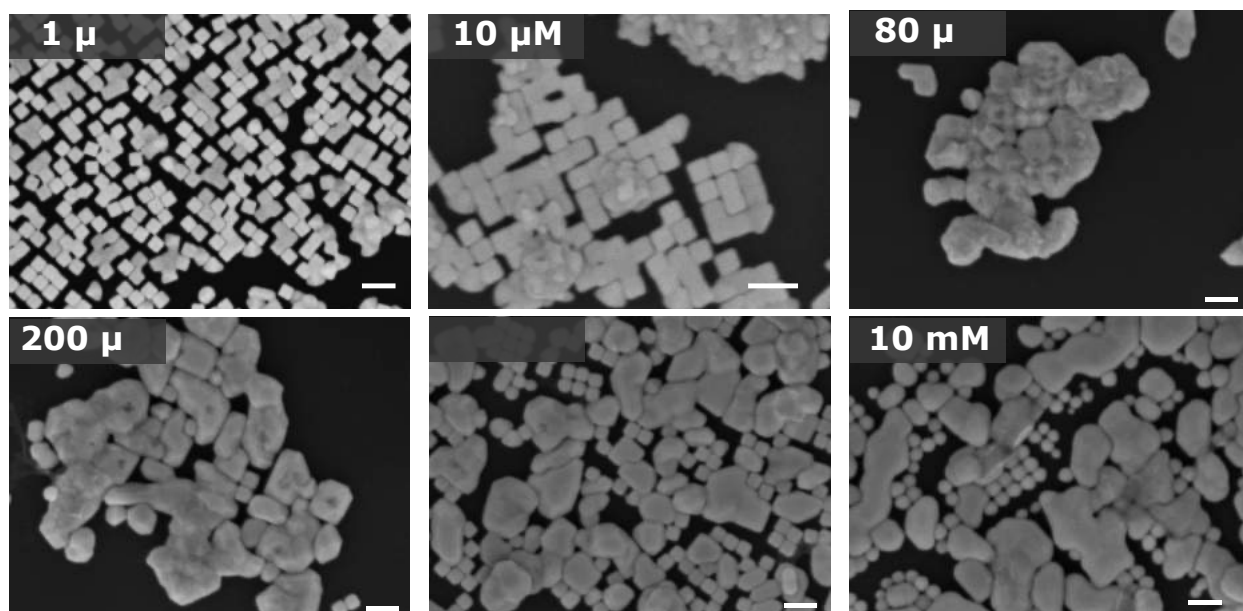


Figure S3: Effect of H[AuCl<sub>4</sub>] concentration on Au nanocubes deposited on a Si substrate. The immersion time was 1h at 40°C, and the pH was adjusted to 4 with HNO<sub>3</sub> (for 1μM and 10μM) or with NaOH (for 200μM, 1mM and 10mM). Scale bars are 100nm.

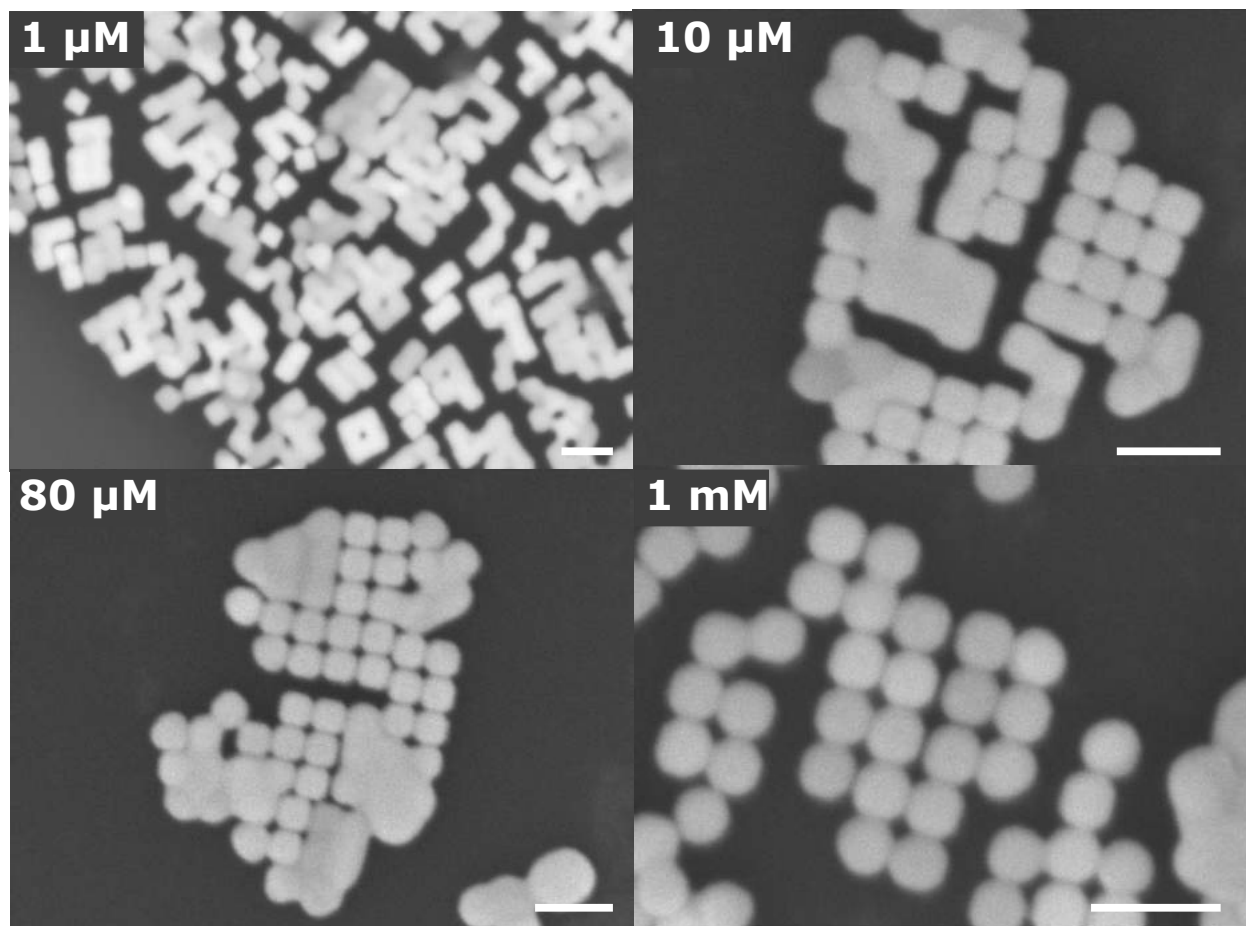


Figure S4: Effect of HAuCl<sub>4</sub> concentration monitored for a pH of 1, to enhance oxidative etching of the nanocubes, at 40°C during an hour, by adjusting the pH with HNO<sub>3</sub> for all concentration. The correlation between HAuCl<sub>4</sub> concentration and oxidative etching of the nanocube corners observed at pH 4 is confirmed. Scale bars are 100nm.

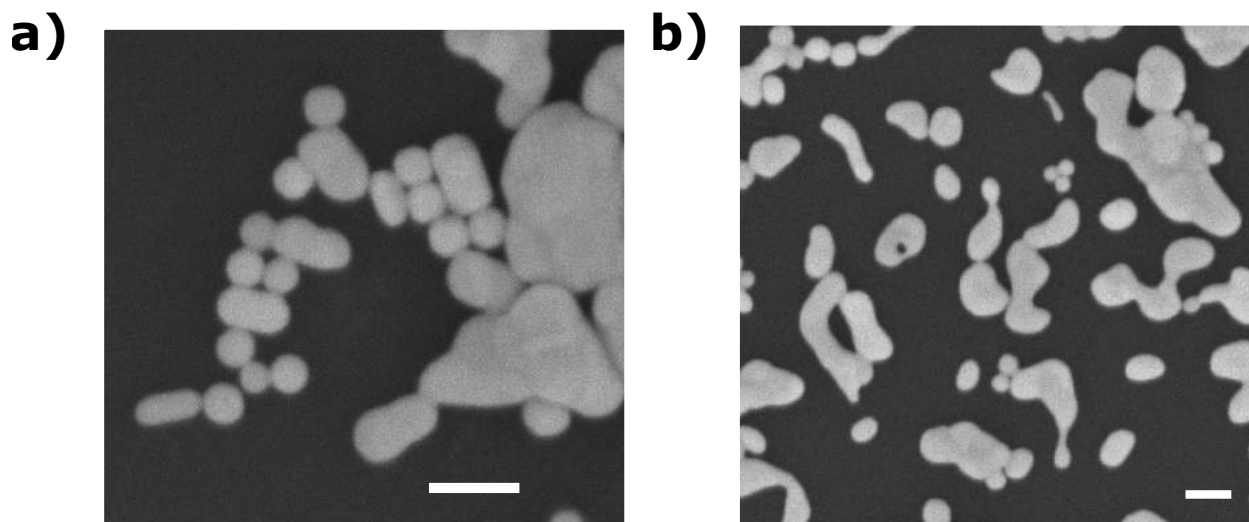


Figure S5: Role of chloride in oxidative etching of the nanocubes. a) NaCl was added to the welding solution composed of  $80\mu\text{M}$   $\text{HAuCl}_4$  only and the reaction was performed at  $40^\circ\text{C}$  during an hour. Rounding of the nanocubes at this concentration shows that adding chloride enhances the dissolution of gold. b) pH of the welding solution ( $80\mu\text{M}$   $\text{HAuCl}_4$ ) is set to 1 using HCl, instead of  $\text{HNO}_3$  generally employed in this study, and the reaction is carried out at  $40^\circ\text{C}$  for an hour. As a result, the nanocubes corners get completely oxidized which confirms the influence of chloride. Scale bars are 100nm.



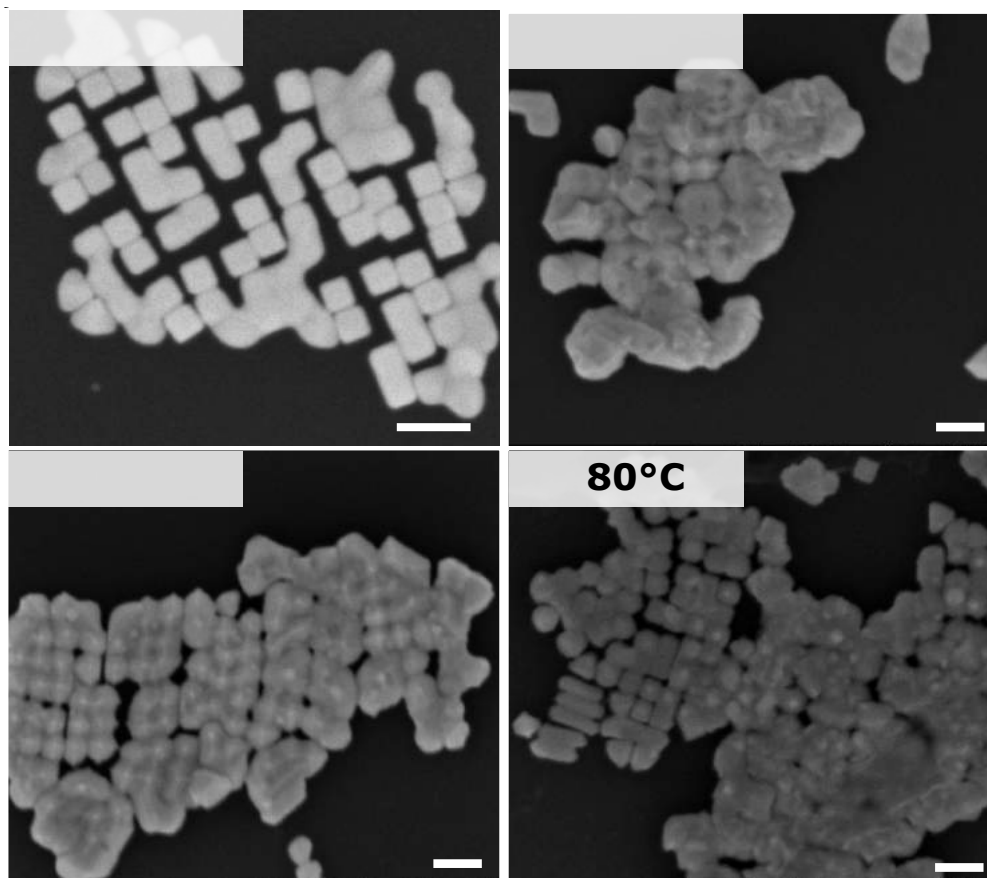


Figure S6: Effect of temperature. Egg-box structure appear when increasing the temperature. Scale bars are 100nm.

**Control experiments** Control experiments showed that the nanocubes dropcasted on silicon and stored in DI water were indeed stable days after ligand removal (Figure S7). When lowering the pH to 4 and increasing the temperature to 40 °C, it was possible to find some evidence of partial welding between adjacent nanocubes after 1h even in the absence of  $\text{HAuCl}_4$  (Figure S8). However, in the presence of  $\text{HAuCl}_4$  within few seconds a stark contrast in the final product was observed, especially in nanocube clusters (Figure S9). This indicates that experimental conditions of pH and temperature alone are not sufficient for consistent nanocube epitaxy.

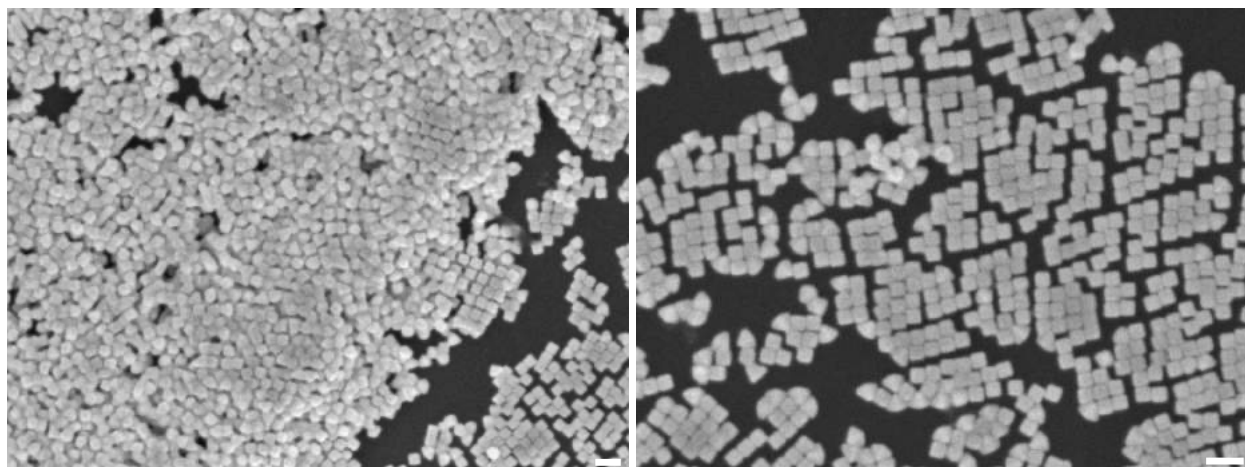


Figure S7: SEM images of gold nanocubes deposited on silicon and stored in water for 4 days after ligands removal, showing that epitaxial welding of nanocubes is not spontaneous upon ligand removal in water and at room temperature. Scale bars are 100nm.

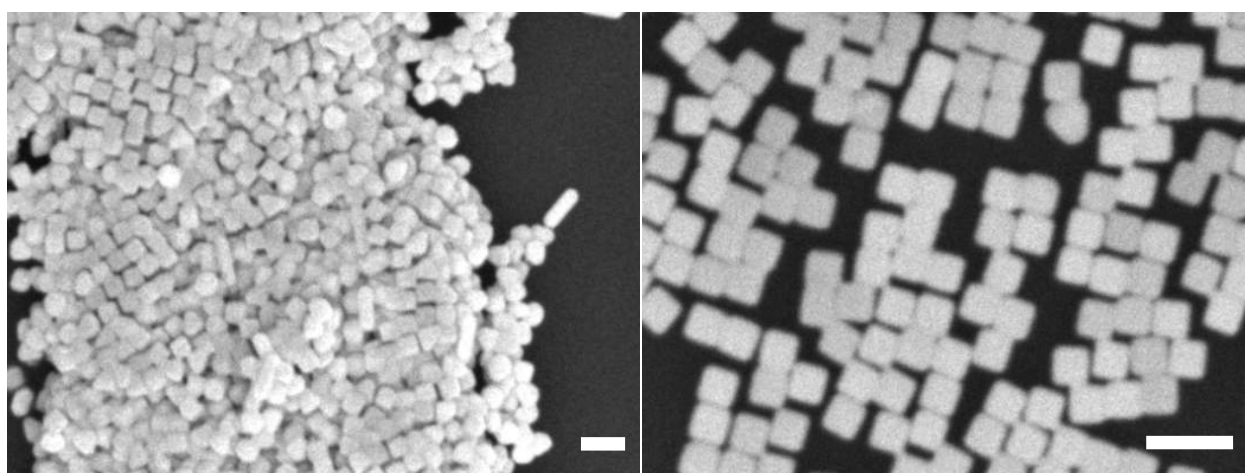


Figure S8: SEM images of silicon supported gold nanocubes after being immersed for 60 minutes in a diluted nitric acid aqueous solution of pH 4 at 40°C after ligand removal. This experiment is used as a control to evidence that temperature and acidic conditions alone are not responsible for the welding of the nanocubes in 80 $\mu$ M HAuCl<sub>4</sub> solution. Scale bars are 100nm.

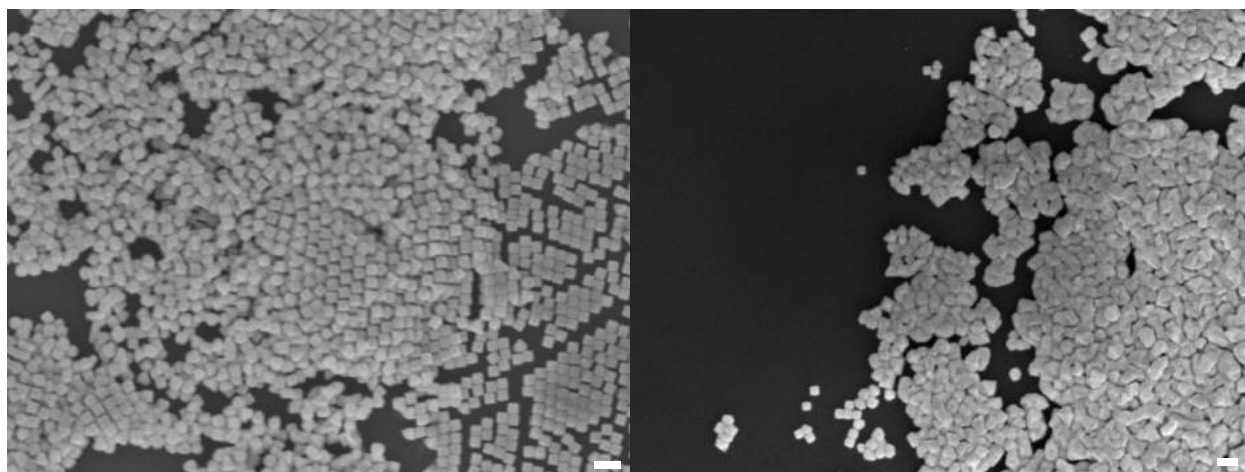


Figure S9: Silicon supported gold nanocubes before and after being immersed in a  $80\mu\text{M}$   $\text{HAuCl}_4$  at  $40^\circ\text{C}$  for one minute, showing that as opposed to organized 1D and 2D assemblies of nanocubes, 3D clusters of gold nanocubes are typically transformed into unrecognizable structures in which nanocubes cannot be identified anymore. Scale bars are 100nm.

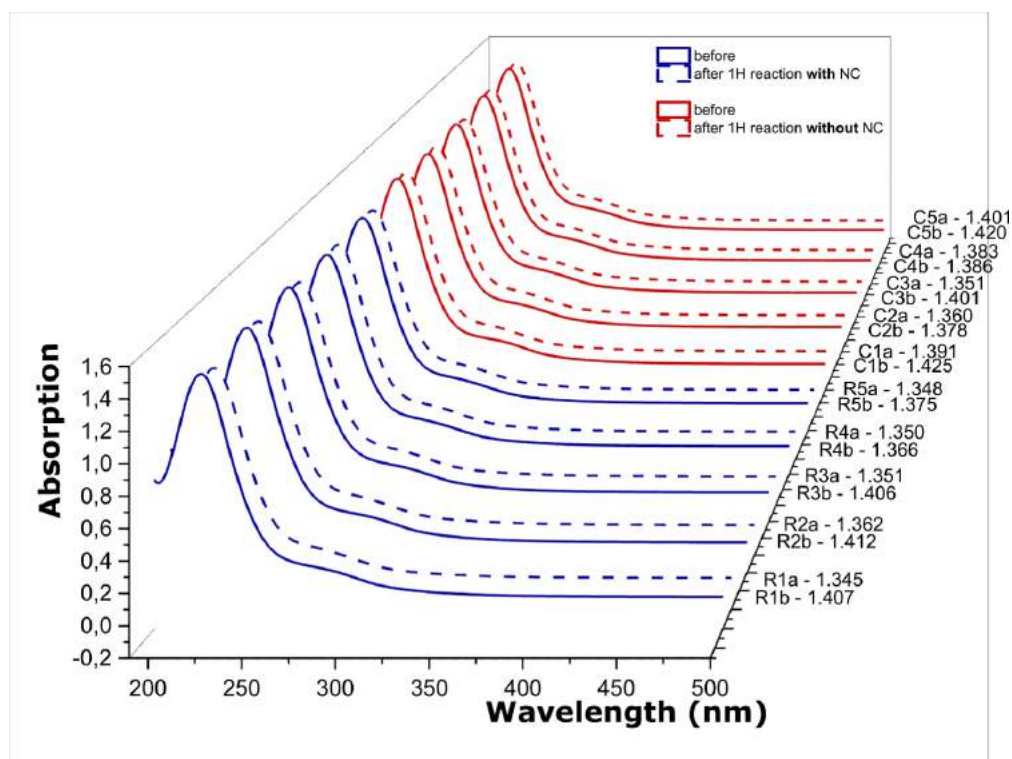


Figure S10: UV-vis spectra of  $80\mu\text{M}$   $\text{HAuCl}_4$  solutions before and after i) reaction with nanocubes for 1 hour at  $40^\circ\text{C}$  (blue curves) and ii) heating the solution at  $40^\circ\text{C}$  without nanocubes (red curves). From this data we can calculate that  $2.4\mu\text{M}$  of  $\text{AuCl}_4^-$  was consumed in the presence of nanocubes and  $1.42\mu\text{M}$  in their absence in average.

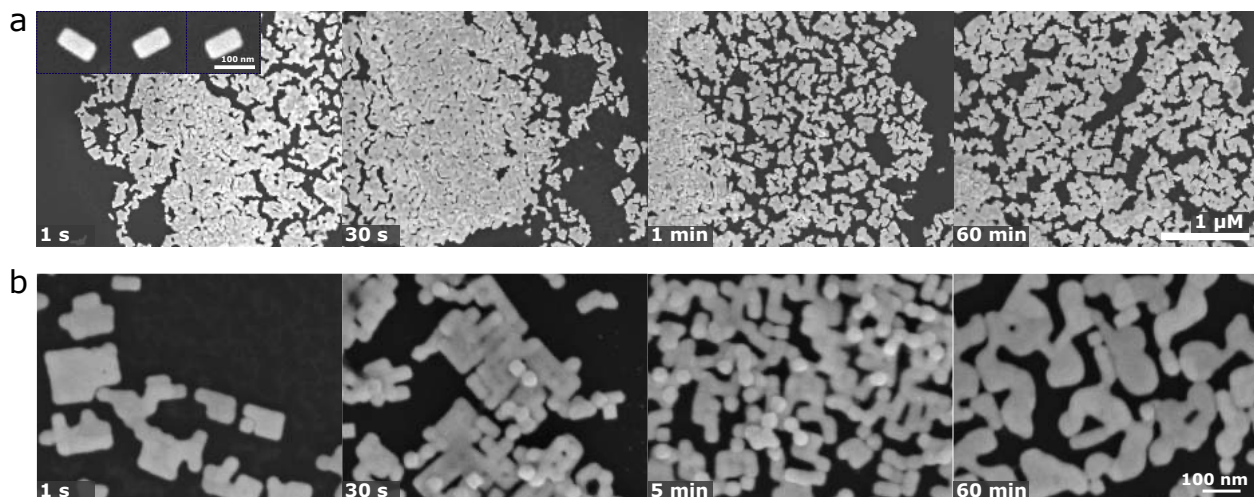


Figure S11: Effect of reaction time. Silicon supported gold nanocubes, free from ligands, are immersed in the  $80\mu\text{M}$   $\text{HAuCl}_4$  welding solution at  $40^\circ\text{C}$  for different times. a) At a pH of 1 (adjusted with  $\text{HNO}_3$ ) for 40-nm nanocubes. Welding of nanocubes is achieved in less than a second as evidenced in the inset. The general morphology of the welded nanostructures and 3D clusters remain similar for different reaction times. b) At a pH of 4 (no pH adjustment) for 32-nm nanocubes. Again, welding of nanocubes is achieved in less than a second and is not improved with time. However, it seems that smaller cubes are more prone to oxidative etching after one hour.

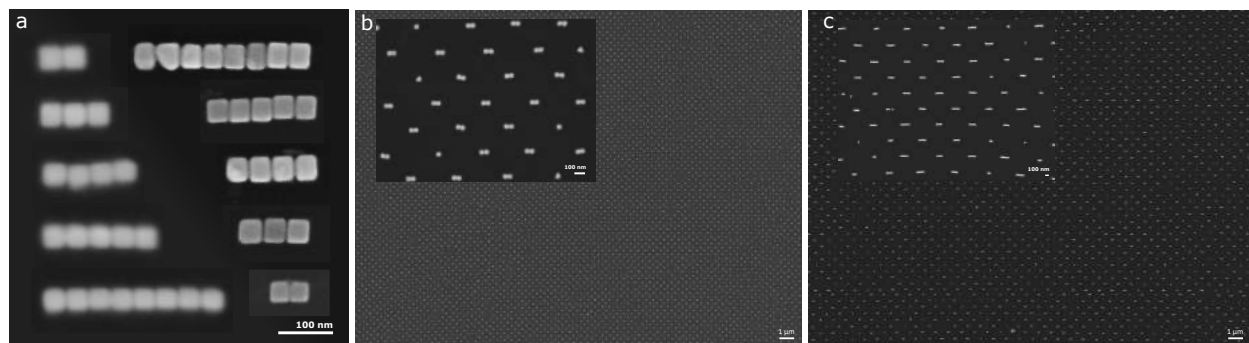


Figure S12: Assembly of nanocubes using capillary assembly. a) assembly of 1D nanostructures of different length in PDMS (left image) and printing on silicon with nanometer accuracy (right image). b) Assembly of nanocubes 2 by 2 (dimers) over large areas. c) Assembly of nanocubes 4 by 4 over large areas.



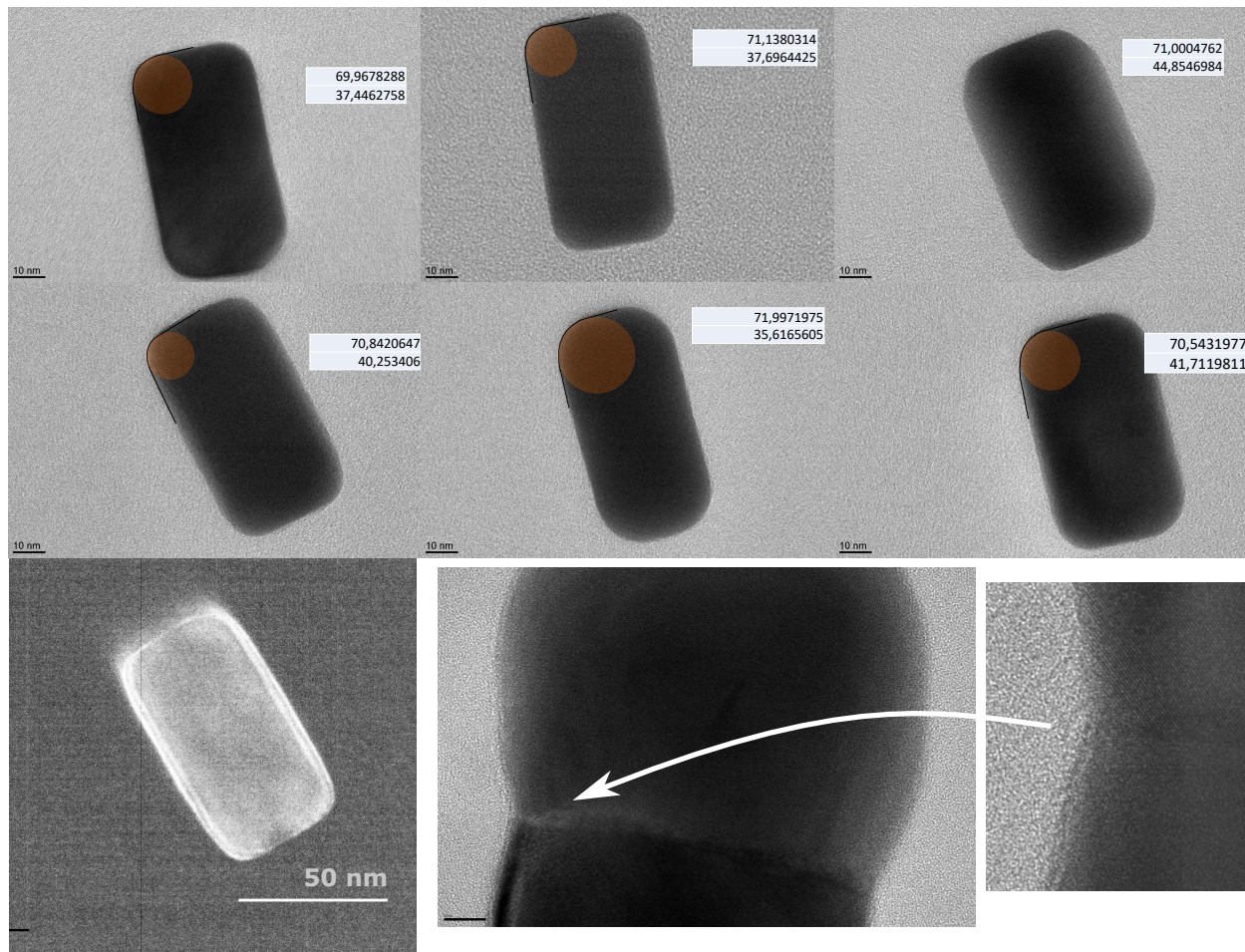


Figure S13: a) TEM images of 35-nm welded dimers printed on  $\text{Si}_3\text{N}_4$  grids. Length and width are indicated on each picture. b) Dark Field image of 40-nm nanocube dimer upon epitaxy in PDMS and printing on a  $\text{Si}_3\text{N}_4$  grid c) Grain boundary resulting from the epitaxial welding of other nanocrystal shapes.

Nanocube dimers (not welded) were printed to a  $\text{Si}_3\text{N}_4$  membrane to characterize via TEM the average gap size, that was found to be 0.4 nm (see Figure S14). After welding, the nanostructures retained their initial length (twice the size of the nanocubes, plus the gap) or were slightly shorter, but systematically grew slightly wider, from 35.5 to 39.5 nm in average in the example given in Figure S13. The bending radius increased from 5.6 to 9.6.

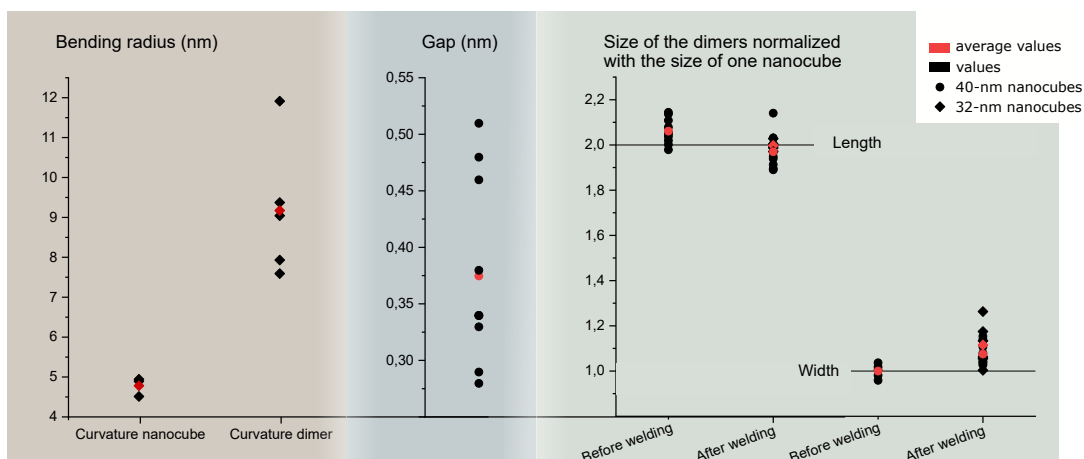


Figure S14: Size, gap and bending radius statistics performed using TEM images of dimers formed using 35 nm and 40 nm nanocubes before and after welding.

## Role of substrate

In order to understand the role played by silicon in the reaction, NC cubes were deposited in i) p-doped silicon ii) n-doped silicon iii) p-doped silicon with Si-OH bonds, created upon oxygen plasma iv) p-doped silicon with Si-H bonds, created upon H-F treatment. While it was possible to epitaxially connect nanocubes into continuous structures on both n and p doped silicon using gold chloride only, nanocubes supported by the oxygen-plasma treated silicon showed no evidence of welding after one hour reaction at 40°C, similarly to glass, Si<sub>3</sub>N<sub>4</sub> and PDMS substrates. H-F treated silicon substrates however exhibited not only nanocube welding but many sites of nucleation and growth (Figure S15). Gold chloride reduction on HF treated silicon has been reported before, although no mechanism was proposed.<sup>59</sup> We hypothesize that the substrate dependent welding that we witnessed between silicon and other substrates come from silicon surface chemistry and the presence of Si-H bonds at its surface.

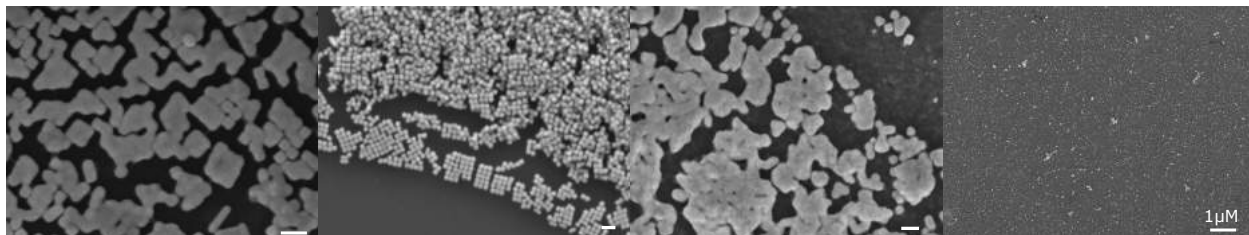


Figure S15: Reaction of different substrates using  $80\mu\text{M}$   $\text{HAuCl}_4$  welding solution at  $40^\circ\text{C}$ . From left to right: n-doped silicon, plasma treated p-doped silicon, welded nanocubes on H-F treated p-doped silicon, nucleation on H-F treated p-doped silicon. Scale bars are 100 nm unless stated otherwise.

## Standard potential calculation

### Concentrations

Concentration of the different species that potentially participate to the welding reaction are calculated using dissociation constants.

$\text{HAuCl}_4$  is a strong acid and so dissociate completely to  $\text{AuCl}_4^-$  and  $\text{H}^+$  in water.  $\text{AuCl}_4^-$  slightly dissociate to  $\text{Cl}^-$  and  $\text{Au}^{3+}$  depending on the temperature.<sup>60</sup> Using table 1 values we calculate  $\text{AuCl}_4^-$ ,  $\text{Cl}^-$  and  $\text{Au}^{3+}$  concentration in the welding solution for different starting concentration  $C_0$ .

Table 1: Log dissociation constants toward  $\text{Au}^{3+}$  and  $\text{Cl}^-$  for the complex  $\text{AuCl}_4^-$ <sup>60</sup>

log K	25°C	50°C	80°C
$\text{AuCl}_4^-$	-25.2	-24.6	-24.3

### Redox couple $\text{O}_2/\text{H}_2\text{O}$



$$E_{\text{O}_2/\text{H}_2\text{O}} = 1.229 - 1.984 \cdot 10^{-4} \times T \times \text{pH} \quad (4)$$

### Redox couple $\text{AuCl}_4^-/\text{Au}$



$$E^0 = 1.002$$

$$E_{\text{AuCl}_4^-/\text{Au}} = E^0 - \left(\frac{RT}{nF}\right) \ln \frac{a_{\text{Cl}^-}^4}{a_{[\text{AuCl}_4]^-}}$$

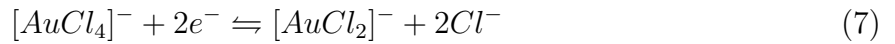
### Redox couple $\text{AuCl}_2^-/\text{Au}$



$$E^0 = 1.154$$

$$E_{\text{AuCl}_2^-/\text{Au}} = E^0 - \left(\frac{RT}{nF}\right) \ln \frac{[\text{Cl}^-]^2}{[\text{AuCl}_2]^-}$$

### Redox couple $\text{AuCl}_4^-/\text{AuCl}_2^-$



$$E^0 = 0.926V$$

$$E_{\text{AuCl}_4^-/\text{AuCl}_2^-} = E^0 + \left(\frac{RT}{nF}\right) \ln \frac{[\text{AuCl}_4]^-}{[\text{AuCl}_2]^- [\text{Cl}^-]^2} \quad (8)$$

### Activities

In order to calculate reaction potential activities ( $a_i$ ) are first calculated for the different species.

$$I = \frac{1}{2} \sum z_i^2 \times C_i \quad (9)$$



The ionic strength ( $I$ ) of the solution is first calculated, using  $z_i$  and  $C_i$ , respectively charge and concentration of the specie. Here we have almsot exclusively  $H^+$  and  $AuCl_4^-$  in solution:

$$I \approx [HAuCl_4]_0 \quad (10)$$

When  $I < 10^{-3}$  M, which is the case for all welding solution, we can use Debye Hückel expression (expression 11) to calculate the activity coefficient (expression 12).

$$\log \gamma_i = -0.51 z_i^2 \sqrt{I} \quad (11)$$

$$a_i = \gamma_i \frac{C_i}{C_0} \quad (12)$$

Where  $\gamma_i$  is the activity coefficient,  $C_i$  concentration of the specie in solution and  $C_0 = 1 \text{ mol.L}^{-1}$ .

Table 2: Activity coefficient and activities as a fonction of initial concentration

$C_0$	1 $\mu\text{M}$	10 $\mu\text{M}$	80 $\mu\text{M}$	200 $\mu\text{M}$	1 mM
$\gamma_i$	0.999	0.996	0.989	0.983	0.963
$a_i$	0.99 $\mu\text{M}$	9.96 $\mu\text{M}$	79.1 $\mu\text{M}$	197 $\mu\text{M}$	963 $\mu\text{M}$

## Reaction potential

Using those values and the concentrations determined above for different temperatures we can calculate that:

- Reduction of  $AuCl_4^-$  to Au happens at potentials between 1.37 and 1.43 V for concentration between 1  $\mu\text{M}$  and 10 mM and temperatures between 25 and 80 °C.
- Reduction of  $AuCl_2^-$  to Au happens at potentials between 1.37 and 1.47 V for concentration between 1  $\mu\text{M}$  and 10 mM and temperatures between 25 and 80 °C.

- Reduction of  $\text{AuCl}_4^-$  to  $\text{AuCl}_2^-$  happens at potentials between 1.36 and 1.42 V for concentration between 1  $\mu\text{M}$  and 10 mM and temperatures between 25 and 80  $^\circ\text{C}$ .

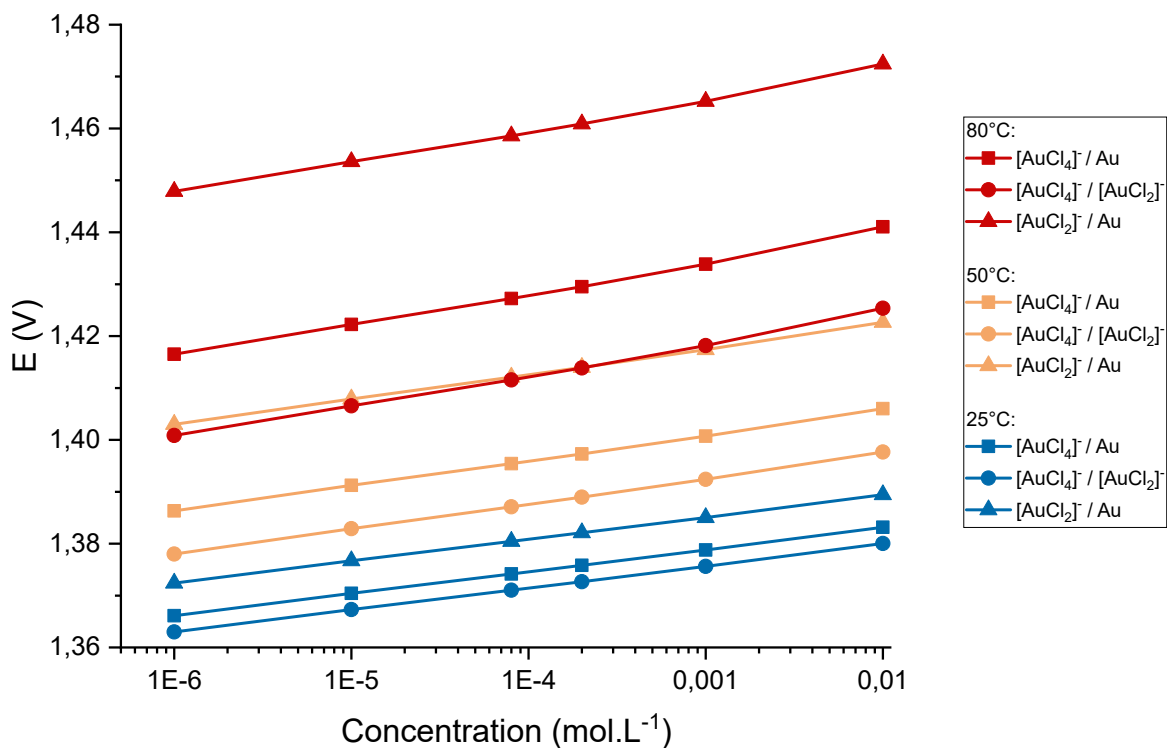


Figure S16: Potential-concentration diagram for different redox couple and temperatures.

## References

1. Garnett, E. C.; Ehrler, B.; Polman, A.; Alarcon-Llado, E. Photonics for Photovoltaics: Advances and Opportunities. *ACS Photonics* **2021**, *8*, 61–70.
2. Koenderink, A. F.; Alù, A.; Polman, A. Nanophotonics: Shrinking light-based technology. *Science* **2015**, *348*, 516–521.
3. Choi, J. H.; Wang, H.; Oh, S. J.; Paik, T.; Jo, P. S.; Sung, J.; Ye, X.; Zhao, T.; Diroll, B. T.; Murray, C. B.; Kagan, C. R. Exploiting the colloidal nanocrystal library to construct electronic devices. *Science* **2016**, *352*, 205–208.

4. Lee, J. K.; Samanta, D.; Nam, H. G.; Zare, R. N. Spontaneous formation of gold nanostructures in aqueous microdroplets. Nature Communications **2018**, 1–9.
5. Maier, S. a. Fundamentals and Applications Plasmonics : Fundamentals and Applications; 2007.
6. Bin-Alam, M. S.; Reshef, O.; Mamchur, Y.; Alam, M. Z.; Carlow, G.; Upham, J.; Sullivan, B. T.; Ménard, J. M.; Huttunen, M. J.; Boyd, R. W.; Dolgaleva, K. Ultra-high-Q resonances in plasmonic metasurfaces. Nature Communications **2021**, 12, 974.
7. Kelly, K. L.; Coronado, E.; Zhao, L. L.; Shatz, G. C. The Optical Properties of Metal Nanoparticles: The Influence of Size, Shape, and Dielectric Environment. Journal of Physical Chemistry B **2003**, 107, 668–677.
8. Keunen, R.; MacOretta, D.; Cathcart, N.; Kitaev, V. Stable ligand-free stellated polyhedral gold nanoparticles for sensitive plasmonic detection. Nanoscale **2016**, 8, 2575–2583.
9. Eustis, S.; El-Sayed, M. A. Why gold nanoparticles are more precious than pretty gold: Noble metal surface plasmon resonance and its enhancement of the radiative and nonradiative properties of nanocrystals of different shapes. Chemical Society Reviews **2006**, 35, 209–217.
10. Baffou, G.; Quidant, R. Nanoplasmonics for chemistry. Chemical Society Reviews **2014**, 43, 3898–3907.
11. Shi, Q.; Connell, T. U.; Xiao, Q.; Chesman, A. S.; Cheng, W.; Roberts, A.; Davis, T. J.; Gómez, D. E. Plasmene Metasurface Absorbers: Electromagnetic Hot Spots and Hot Carriers. ACS Photonics **2019**, 6, 314–321.
12. Nie, S.; Emory, S. R. Probing single molecules and single nanoparticles by surface-enhanced Raman scattering. Science **1997**, 275, 1102–1106.

13. Willets, K. A.; Van Duyne, R. P. Localized surface plasmon resonance spectroscopy and sensing. Annual Review of Physical Chemistry **2007**, 58, 267–297.
14. Nuñez, J.; Boersma, A.; Grand, J.; Mintova, S.; Sciacca, B. Thin Functional Zeolite Layer Supported on Infrared Resonant Nano-Antennas for the Detection of Benzene Traces. Advanced Functional Materials **2021**, 31, 2101623.
15. Cortés, E.; Xie, W.; Cambiasso, J.; Jermyn, A. S.; Sundararaman, R.; Narang, P.; Schlücker, S.; Maier, S. A. Plasmonic hot electron transport drives nano-localized chemistry. Nature Communications **2017**, 8, 14880.
16. Navlani-García, M.; Salinas-Torres, D.; Mori, K.; Kuwahara, Y.; Yamashita, H. Tailoring the Size and Shape of Colloidal Noble Metal Nanocrystals as a Valuable Tool in Catalysis. Catalysis Surveys from Asia **2019**, 23, 127–148.
17. Linic, S.; Aslam, U.; Boerigter, C.; Morabito, M. Photochemical transformations on plasmonic metal nanoparticles. Nature Materials **2015**, 14, 567–576.
18. Anker, J. N.; Hall, W. P.; Lyandres, O.; Shah, N. C.; Zhao, J.; Duyne, R. P. V. Biosensing with plasmonic nanosensors. Nature Materials **2008**, 7, 442—453.
19. Yang, X.; Yang, M.; Pang, B.; Vara, M.; Xia, Y. Gold Nanomaterials at Work in Biomedicine. Chemical Reviews **2015**, 115, 10410–10488.
20. Atwater, H. A.; Polman, A. Plasmonics for improved photovoltaic devices. Nature Materials **2010**, 9, 205–213.
21. Oksenberg, E.; Shlesinger, I.; Xomalis, A.; Baldi, A.; Baumberg, J. J.; Koenderink, A. F.; Garnett, E. C. Energy-resolved plasmonic chemistry in individual nanoreactors. Nature Nanotechnology **2021**,
22. Won, R. The rise of plasmonic metasurfaces. Nature Photonics **2017**, 11, 462–464.

23. Biswas, A.; Bayer, I. S.; Biris, A. S.; Wang, T.; Dervishi, E.; Faupel, F. Advances in top-down and bottom-up surface nanofabrication: Techniques, applications & future prospects. Advances in Colloid and Interface Science **2012**, 170, 2–27.
24. Wu, Y.; Zhang, C.; Estakhri, N. M.; Zhao, Y.; Kim, J.; Zhang, M.; Liu, X.-X.; Pribil, G. K.; Alù, A.; Shih, C.-K.; Li, X. Intrinsic Optical Properties and Enhanced Plasmonic Response of Epitaxial Silver. Advanced Materials **2014**, 26, 6106–6110.
25. Capitaine, A.; Sciacca, B. Monocrystalline Methylammonium Lead Halide Perovskite Materials for Photovoltaics. Advanced Materials **2021**, n/a, 2102588.
26. Nagpal, P.; Lindquist, N. C.; Oh, S.-H.; Norris, D. J. Ultrasoother Patterned Metals for Plasmonics and Metamaterials. Science **2009**, 325, 594–597.
27. Zhang, H.; Kinnear, C.; Mulvaney, P. Fabrication of Single-Nanocrystal Arrays. Advanced Materials **2020**, 32, 1904551.
28. Park, J. E.; Lee, Y.; Nam, J. M. Precisely Shaped, Uniformly Formed Gold Nanocubes with Ultrahigh Reproducibility in Single-Particle Scattering and Surface-Enhanced Raman Scattering. Nano Letters **2018**, 18, 6475–6482.
29. Yoreo, J. J. D.; Gilbert, P. U. P. A.; Sommerdijk, N. A. J. M.; Penn, R. L.; Whitlam, S.; Joester, D.; Zhang, H.; Rimer, J. D.; Navrotsky, A.; Banfield, J. F.; Wallace, A. F.; Michel, F. M.; Meldrum, F. C.; Cölfen, H.; Dove, P. M. Crystallization by particle attachment in synthetic, biogenic, and geologic environments. Science **2015**, 349, aaa6760.
30. Millstone, J. E.; Wei, W.; Jones, M. R.; Yoo, H.; Mirkin, C. A. Iodide ions control seed-mediated growth of anisotropic gold Nanoparticles. Nano Letters **2008**, 8, 2526–2529.
31. Sciacca, B.; Berkhout, A.; Brenny, B. J.; Oener, S. Z.; van Huis, M. A.; Polman, A.; Garnett, E. C. Monocrystalline Nanopatterns Made by Nanocube Assembly and Epitaxy. Advanced Materials **2017**, 29, 1701064.

32. Yang, H. J.; He, S. Y.; Chen, H. L.; Tuan, H. Y. Monodisperse copper nanocubes: Synthesis, self-assembly, and large-area dense-packed films. Chemistry of Materials **2014**, 26, 1785–1793.
33. Clark, B. D.; Jacobson, C. R.; Lou, M.; Renard, D.; Wu, G.; Bursi, L.; Ali, A. S.; Swearer, D. F.; Tsai, A. L.; Nordlander, P.; Halas, N. J. Aluminum Nanocubes Have Sharp Corners. ACS Nano **2019**, 13, 9682–9691.
34. Wang, Y.; Zheng, Y.; Huang, C. Z.; Xia, Y. Synthesis of Ag nanocubes 18-32 nm in edge length: The effects of polyol on reduction kinetics, size control, and reproducibility. Journal of the American Chemical Society **2013**, 135, 1941–1951.
35. Kuo, C. H.; Chen, C. H.; Huang, M. H. Seed-mediated synthesis of monodispersed Cu<sub>2</sub>O nanocubes with five different size ranges from 40 to 420 nm. Advanced Functional Materials **2007**, 17, 3773–3780.
36. Chen, H. S.; Wu, S. C.; Huang, M. H. Direct synthesis of size-tunable PbS nanocubes and octahedra and the pH effect on crystal shape control. Dalton Transactions **2014**, 44, 15088–15094.
37. Imran, M.; Ijaz, P.; Baranov, D.; Goldoni, L.; Petralanda, U.; Akkerman, Q.; Abdelhady, A. L.; Prato, M.; Bianchini, P.; Infante, I.; Manna, L. Shape-Pure, Nearly Monodispersed CsPbBr<sub>3</sub> Nanocubes Prepared Using Secondary Aliphatic Amines. Nano Letters **2018**, 18, 7822–7831.
38. Dang, F.; Mimura, K. I.; Kato, K.; Imai, H.; Wada, S.; Haneda, H.; Kuwabara, M. Growth of monodispersed SrTiO<sub>3</sub> nanocubes by thermohydrolysis method. CrystEngComm **2011**, 13, 3878–3883.
39. Joshi, U. A.; Jang, J. S.; Borse, P. H.; Lee, J. S. Microwave synthesis of single-crystalline perovskite BiFeO<sub>3</sub> nanocubes for photoelectrode and photocatalytic applications. Applied Physics Letters **2008**, 92, 2006–2009.

40. Yang, S.; Gao, L. Controlled Synthesis and Self-Assembly of CeO<sub>2</sub> Nanocubes. Journal of the American Chemical Society **2006**, 128, 9330–9331.
41. Haggui, M.; Dridi, M.; Plain, J.; Marguet, S.; Perez, H.; Schatz, G. C.; Wiederrecht, G. P.; Gray, S. K.; Bachelot, R. Spatial confinement of electromagnetic hot and cold spots in gold nanocubes. ACS Nano **2012**, 6, 1299–1307.
42. Ansar, S. M.; Ameer, F. S.; Hu, W.; Zou, S.; Pittman, C. U.; Zhang, D. Removal of Molecular Adsorbates on Gold Nanoparticles Using Sodium Borohydride in Water. Nano Letters **2013**, 13, 1226–1229.
43. Ni, S.; Leemann, J.; Buttinoni, I.; Isa, L.; Wolf, H. Programmable colloidal molecules from sequential capillarity-assisted particle assembly. Science Advances **2016**, 2, e1501779.
44. Flauraud, V.; Mastrangeli, M.; Bernasconi, G. D.; Butet, J.; Alexander, D. T.; Shahrabi, E.; Martin, O. J.; Brugger, J. Nanoscale topographical control of capillary assembly of nanoparticles. Nature Nanotechnology **2017**, 12, 73–80.
45. Kraus, T.; Malaquin, L.; Schmid, H.; Riess, W.; Spencer, N. D.; Wolf, H. Nanoparticle printing with single-particle resolution. Nature Nanotechnology **2007**, 2, 570–576.
46. Malaquin, L.; Kraus, T.; Schmid, H.; Delamarche, E.; Wolf, H. Controlled particle placement through convective and capillary assembly. Langmuir **2007**, 23, 11513–11521.
47. Ni, S.; Isa, L.; Wolf, H. Capillary assembly as a tool for the heterogeneous integration of micro- and nanoscale objects. Soft Matter **2018**, 14, 2978–2995.
48. King, M. E.; Kent, I. A.; Personick, M. L. Halide-assisted metal ion reduction: emergent effects of dilute chloride, bromide, and iodide in nanoparticle synthesis. Nanoscale **2019**, 11, 15612–15621.

49. Knebl, D.; Hörl, A.; Trügler, A.; Kern, J.; Krenn, J. R.; Puschnig, P.; Hohenester, U. Gap plasmonics of silver nanocube dimers. Phys. Rev. B **2016**, 93, 081405.
50. Oh, M. H.; Cho, M. G.; Chung, D. Y.; Park, I.; Kwon, Y. P.; Ophus, C.; Kim, D.; Kim, M. G.; Jeong, B.; Gu, X. W.; Jo, J.; Yoo, J. M.; Hong, J.; McMains, S.; Kang, K.; Sung, Y.-E.; Alivisatos, A. P.; Hyeon, T. Design and synthesis of multigrain nanocrystals via geometric misfit strain. Nature **2020**, 577, 359–363.
51. Mariano, R. G.; McKelvey, K.; White, H. S.; Kanan, M. W. Selective increase in CO<sub>2</sub> electroreduction activity at grain-boundary surface terminations. Science **2017**, 358, 1187–1192.
52. Yoon, S.; Kim, C.; Lee, B.; Lee, J. H. From a precursor to an etchant: spontaneous inversion of the role of Au(III) chloride for one-pot synthesis of smooth and spherical gold nanoparticles. Nanoscale Adv. **2019**, 1, 2157–2161.
53. Seisko, S.; Lampinen, M.; Aromaa, J.; Laari, A.; Koironen, T.; Lundström, M. Kinetics and mechanisms of gold dissolution by ferric chloride leaching. Minerals Engineering **2018**, 115, 131–141.
54. Nicol, M. J. The anodic behaviour of gold - Part II - Oxidation in alkaline solutions. Gold Bulletin **1980**, 13, 105–106.
55. Peck, J. A.; Tait, C. D.; Swanson, B. I.; Brown, G. E. Speciation of aqueous gold(III) chlorides from ultraviolet/visible absorption and Raman/resonance Raman spectroscopies. Geochimica et Cosmochimica Acta **1991**, 55, 671–676.
56. Gammons, C. H.; Yu, Y. The disproportionation of gold ( I ) chloride complexes at 25 to 200 ° C. Geochimica et Cosmochimica Acta **1997**, 61, 1971–1983.
57. Vargas-Hernandez, C.; Mariscal, M. M.; Esparza, R.; Yacaman, M. J. A synthesis route of



- gold nanoparticles without using a reducing agent A synthesis route of gold nanoparticles without using a reducing agent. Applied Physics Letters **2010**, 96, 2013115.
58. In situ synthesis of directional gold nanoparticle arrays along ridge cracks of PDMS wrinkles. Colloids and Surfaces A: Physicochemical and Engineering Aspects **2018**, 558, 186–191.
59. Sun, L.; Chen, Y.; Gong, F.; Dang, Q.; Xiang, G.; Cheng, L.; Liao, F.; Shao, M. Silicon nanowires decorated with gold nanoparticles via in situ reduction for photoacoustic imaging-guided photothermal cancer therapy. Journal of Materials Chemistry B **2019**, 7, 4393–4401.
60. Usher, A.; Mcphail, D. C. A spectrophotometric study of aqueous Au ( III ) halide – hydroxide complexes at 25 – 80°C. Geochimica et Cosmochimica **2009**, 73, 3359–3380.